Intercomparison and Validation of Techniques for Spectral Unmixing of Hyperspectral Images: A Planetary Case Study

Xavier Ceamanos, *Student Member, IEEE*, Sylvain Douté, Bin Luo, Frédéric Schmidt, Gwenaël Jouannic, and Jocelyn Chanussot, *Senior Member, IEEE*

***Abstract*—As the volume of hyperspectral data for planetary exploration increases, efficient yet accurate algorithms are decisive for their analysis. In this paper, the capability of spectral unmixing for analyzing hyperspectral images from Mars is investigated. For that purpose, we consider the Russell megadune observed by the Compact Reconnaissance Imaging Spectrometer for Mars (CRISM) and the High-Resolution Imaging Science Experiment (HiRISE) instruments. In late winter, this area of Mars is appropriate for testing linear unmixing techniques because of the geographical coexistence of seasonal CO_2 ice and defrosting dusty features that is not resolved by CRISM. Linear unmixing is carried out on a selected CRISM image by seven state-of-the-art approaches based on different principles. Three physically coherent sources with an increasing fingerprint of dust are recognized by the majority of the methods. Processing of HiRISE imagery allows the construction of a ground truth in the form of a reference abundance map related to the defrosting features. Validation of abundances estimated by spectral unmixing is carried out in an independent and quantitative manner by comparison with the ground truth. The quality of the results is estimated through the correlation coefficient and average error between the reconstructed and reference abundance maps. Intercomparison of the selected linear unmixing approaches is performed. Global and local comparisons show that misregistration inaccuracies between the HiRISE and CRISM images represent the major source of error. We also conclude that abundance maps provided by three methods out of seven are generally accurate, i.e., sufficient for a planetary interpretation.**

Manuscript received October 22, 2010; revised February 2, 2011; accepted March 30, 2011. Date of publication May 19, 2011; date of current version October 28, 2011. This work was done within the framework of the Vahiné project funded by the "Agence Nationale de la Recherche" (ANR) and the "Centre National d'Études Spatiales" (CNES). We also acknowledge support from the "Centre National de la Recherche Scientifique" (CNRS) through the "Programme National de Planétologie."

X. Ceamanos and S. Douté are with the Institut de Planétologie et d'Astrophysique de Grenoble (IPAG), UJF-CNRS, UMR 5274, 38041 Grenoble, France (e-mail: xavier.ceamanos@obs.ujf-grenoble.fr; sylvain.doute@obs.ujf-grenoble.fr).

B. Luo is with the Gipsa-lab, Grenoble Institute of Technology, 38402 Grenoble, France and also with the State Key Laboratory of Information Engineering in Surveying, Mapping and Remote Sensing (LIESMARS), Wuhan University, Wuhan 430079, China (e-mail: robinlb2002@gmail.com).

F. Schmidt is with the Université Paris-Sud, Laboratoire IDES, UMR 8148 and CNRS, 91405 Orsay, France (e-mail: frederic.schmidt@u-psud.fr).

G. Jouannic is with the Université Paris-Sud, Laboratoire IDES, UMR 8148 and CNRS, 91405 Orsay, France and also with the International Research School of Planetary Sciences, Università G. d'Annunzio, 65127 Pescara, Italy (e-mail: gwenael.jouannic@u-psud.fr).

J. Chanussot is with the Gipsa-lab, Grenoble Institute of Technology, 38402 Grenoble, France (e-mail: jocelyn.chanussot@gipsa-lab.grenoble-inp.fr).

Color versions of one or more of the figures in this paper are available online at http://ieeexplore.ieee.org.

Digital Object Identifier 10.1109/TGRS.2011.2140377

***Index Terms*—Blind source separation, Compact Reconnaissance Imaging Spectrometer for Mars (CRISM), ground truth, High-Resolution Imaging Science Experiment (HiRISE), hyperspectral imagers, Mars, remote sensing of planetary surfaces, spectral analysis, unsupervised linear unmixing.**

I. Introduction

VISIBLE and near-infrared imaging spectroscopy is a key remote sensing technique to study planetary objects. Since their first appearance in 1989, imaging spectrometers have been aboard an increasing number of orbiters aimed at exploring our solar system. This kind of sensors have been decisive when addressing issues related to the surface or the atmosphere of Mars, Venus, Jupiter, Saturn, and their moons [1]–[5]. In particular, imaging spectroscopy gives outstanding results regarding the chemical composition and physical state of solid surfaces, thus providing clues about present and past activity and environmental conditions. Constant technological improvements promote the acquisition of dramatically expending collections of hyperspectral images. For instance, the Compact Reconnaissance Imaging Spectrometer for Mars (CRISM) aboard Mars Reconnaissance Orbiter (MRO) is the first hyperspectral imager to operate systematically in multiangle mode at high spatial resolution from orbit [1].

Because of the increasing volume and complexity of planetary hyperspectral data such as CRISM's, efficient yet accurate algorithms are decisive for their analysis. Unsupervised spectral unmixing techniques are potentially relevant tools, particularly in planetary sciences for which only few ground truth data are available. These techniques aim at separating the existent mixtures between the different contributions—coming mainly from materials at the surface—that form the remotely sensed signal. Materials (i.e., physical sources) at the surface are characterized by their spectral signatures determined by their intrinsic chemical composition. Due to limitations of sensor spatial resolution and multiple scattering of solar photons occurring among distinct physical sources, different spectral signatures may be combined both linearly (i.e., geographic mixtures) and nonlinearly (e.g., intimate mixtures).

First attempts in applying spectral unmixing techniques to planetary hyperspectral data are based on a linear model of the signal, even though nonlinear processes might prevail. The Independent Component Analysis (ICA) has been proposed to extract the existent spectral components (i.e., endmembers) in a hyperspectral image by assuming that physical sources are

0196-2892/$26.00 © 2011 IEEE

non-Gaussian and mutually independent. Application of ICA on images acquired by the Observatoire pour la Minéralogie, l'Eau, les Glaces et l'Activité (OMEGA) hyperspectral imager allows the retrieval of meaningful endmembers in [6]. Likewise, spectra measured by the Visible and Infrared Thermal Imaging Spectrometer (VIRTIS) on the nightside of Venus are analyzed with ICA in [7]. In that study, several extracted endmembers are related to physical components or processes due to good correlation of the corresponding distribution maps with known structures of the Venusian atmosphere. Nonetheless, the role of ICA to carry out spectral unmixing is questioned in [8] since the independence of abundance distributions is not satisfied. Another important limitation of ICA is the potential unphysical results in the form of negative values affecting the extracted spectra or abundances. On the other hand, for more than a decade, the Non-negative Matrix Factorization (NMF) has been an alternative method to solve the unmixing problem under a linear model with non-negative constraint [9]. For instance, the NMF approach has been used in planetary exploration to estimate the surface composition of Mars using data acquired by the Martian rovers [10]. Likewise, the NMF problem has been solved in a Bayesian framework through the Bayesian Positive Source Separation (BPSS) [11] ensuring a unique robust solution. In [12], a combination of spatial ICA and BPSS applied on OMEGA data leads to endmembers whose associated spectra and abundance maps correlate satisfactorily with reference signatures and outcomes of physical models, respectively.

In terrestrial remote sensing, many approaches have been proposed as efficient tools for linear unmixing of hyperspectral data. These methods include the Vertex Component Analysis (VCA) [13] which retrieves the spectra of the existent endmembers by extracting the extrema of the simplex formed by the hyperspectral data. In [14], this geometric method is performed on OMEGA data from Mars with satisfactory results. Similarly to VCA, the widely used N-FINDR [15] algorithm is proposed for endmember extraction of linearly mixed data, showing notable performances on many types of hyperspectral data such as CRISM's in [16]. Contrary to VCA and N-FINDR that require the existence of pure pixels in the data, many methods have been developed without the pure pixel assumption. This is the case of the techniques referred to as Minimum Volume Constrained Non-negative Matrix Factorization (MVC-NMF), Minimum Volume Enclosing Simplex (MVES), and Simplex Identification via Split Augmented Lagrangian (SISAL), which are proposed for endmember extraction of highly mixed data. MVC-NMF decomposes mixed pixels based on the NMF and a minimum volume constraint and has proved to be very efficient on simulated and real data and less sensitive to the estimated number of endmembers [17]. In the same way, MVES proposes a convex analysis by minimizing the simplex volume subject to the constraint that all dimension-reduced pixels are enclosed in it [18]. Eventually, SISAL [19] has been recently proposed to solve the linear unmixing problem based on a non-convex optimization problem with convex constraints [19]. Last but not least, many studies have recently addressed the inclusion of spatial information into endmember extraction [20], [21]. For instance, the authors of [21] propose a spatial preprocessing that enhances the search for endmembers in the unmixing problem. This procedure has proved to provide better extracted spectra and more relevant abundance maps after combination with a traditional endmember extraction method.

In this paper, we propose to evaluate the suitability of spectral unmixing techniques in a planetary context by testing the following comprehensive selection of state-of-the-art algorithms: BPSS, VCA, N-FINDR, MVC-NMF, MVES, and SISAL. In addition, spatial information is integrated into the unmixing process by considering the spatial preprocessing proposed in [21]. In this way, a large scope of methods based on geometric, Bayesian, and spectro-spatial first principles is considered. Unfortunately, the validation of spectral unmixing techniques is a very challenging yet crucial issue, particularly in planetary sciences due to the scarcity of ground truth. In that matter, previous studies traditionally address the validation of unmixing outcomes either through comparison of endmember spectra extracted from real data with reference spectral signatures [22], [23] or by using simulated data [20], [21], [24]. As for abundance maps obtained from unmixing of real data, only the authors of [20] perform their validation by comparing these outcomes with a reference. In that study, reference abundance maps are built from reference spectra manually extracted from the original image. To our knowledge, the validation of spectral unmixing techniques applied on real data through the evaluation of extracted abundance maps in an independent and quantitative manner has never been addressed. We therefore propose an innovative case study that overcomes this hurdle by choosing a CRISM image displaying the Russell dune of Mars. In late winter, this particular area is very suitable for validation of spectral unmixing techniques under a linear model due to two principal reasons: (i) The very likely existence of geographic subpixel mixtures coming from the two predominant materials at the surface and (ii) the possibility of building a ground truth for validation of extracted abundance maps using very high-resolution imagery and geomorphological techniques. Based on original experimentations, we perform quantitative assessment of surface proportions obtained by spectral unmixing techniques on real hyperspectral data. In addition, an intercomparison of the selected unmixing methods is carried out by evaluating their spectral and spatial outcomes independently. Eventually, the linear mixing model and the limitations of the assumptions made by the algorithms are evaluated for the problem at hand.

This paper is organized as follows. In Section II, we present the case study of the Russell dune through the description of the area of interest, the data sets that are used, and the construction of the ground truth. Then, the selection of spectral unmixing algorithms is briefly described in Section III by highlighting the properties of each method that may be suitable for our case study. Likewise, the techniques used for estimating the number of endmembers are introduced. Experiments are carried out in Section IV followed by the intercomparison and validation of the unmixing methods in Section V. Section VI concludes by discussing on the proposed methodology based on unmixing techniques and preprocessing, drawing some conclusions on the potential of unmixing techniques for planetary sciences, and giving some indications for further research.

II. Case Study: The Russell Crater Megadune

A. Description of the Area

The selected area of study is the megadune in the Russell crater of Mars (55° S 12° E). This 134-km wide crater hosts a 1700 km^2 dune field with an uncommon large dune on its northeastern part. This megadune is about 500 m high, 20 km wide, and 40 km long. In particular, the southwest facing scarp of the dune displays many defrosting features in late winter when the retreat of CO_2 ice starts. These phenomena in the form of dark spots—mostly on the top of the dune—and dark elongated patterns—all over the scarp—precede the global sublimation of the ice, eventually uncovering the sandy mineral substratum [25]. The defrosting features as well as the gullies are an ongoing key research topic for the understanding of Mars geology and activity.

The Russell dune represents a potential benchmark for testing spectral unmixing algorithms in a planetary context. During the MRO mission, this area of Mars has been extensively scrutinized in a coordinated manner by very high-resolution imagery and imaging spectroscopy. In late winter, the former fully resolves the geographical coexistence of dark features—mostly made of dust—and brighter ice while the latter does not. Hence, the assumption of linear mixing in the hyperspectral signal coming from the contributions of both components is very reasonable. In addition, the use of very high-resolution imagery can be used for constructing a ground truth against which abundance maps provided by unmixing techniques applied to hyperspectral images can be evaluated.

B. CRISM Data

In the targeted mode, the CRISM instrument maps the mineralogy of Martian key areas at high spectral (362–3920 nm, 6.5 nm/channel) and spatial (up to 18 m/pix) resolution [1]. CRISM offers a new insight into the planet Mars because of its high resolution and its multi-angle capabilities provided by its gimbaled optical sensor unit (OSU). In this way, each targeted observation is composed of a central hyperspectral image at full spatial resolution and a sequence of ten bracketing spatially binned images that are acquired before and after MRO flies over the target.

In July 2009, CRISM had scanned the Russell megadune 15 times of which 4 in late winter when the CO_2 sublimation starts and the defrosting features appear. We therefore select the central image of the targeted observation frt000042aa covering an area of 80 km^2, in which the southern facing scarp of the Russell dune is visible (see Fig. 1). Due to the OSU functioning, this image was acquired with view zenith angles (VZA) varying by more than 60° from the first to the last image row.

1) Preprocessing: Before the unmixing stage, the test image frt000042aa is processed to get rid of the contributions that are not related to the components at the surface. In particular, these contributions may introduce nonlinearities in the data affecting the linear mixture model of the signal. In this way, the test image is corrected for instrumental artifacts, atmospheric effects, and photometric issues. First, residual stripes and spikes are corrected as in [26]. Likewise, the spectral smile effect affecting CRISM images is corrected by the method in [27]. This step is particularly challenging due to the presence of CO_2 ice, which results in a higher strength of the smile artifacts. Second, the contribution of the Martian atmosphere, which is mainly composed by CO_2 gas and mineral aerosols, is corrected as in [28], [29]. The widely used volcano scan algorithm for CRISM data in [30] is not applicable as it does not operate for icy surfaces nor corrects it for aerosol contribution. Imprecisions in the adopted scattering properties of the aerosols as a function of VZA may induce atmospheric residues in the upper and lower rows of the image by means of spurious spectral slopes. Third, atmospherically corrected spectra are transformed into apparent reflectance units R in a similar way as it is done in [1]. For this photometric correction, we take into account the average illumination conditions on the whole scarp by means of the solar zenith angle (SZA). The average SZA of the scarp is retrieved by using a digital terrain model (DTM) of the Russell dune generated by the High-Resolution Imaging Science Experiment (HiRISE) camera. This procedure results in better levels of R for the majority of the spectra when compared to the traditional procedure in which the surface is approximated by the Martian areoid [1]. A complete pixel-wise photometrical correction is not realizable due to noise in the DTM. Likewise, a procedure based on clustering the image according to SZA had to be abandoned as the spatial information coming from the surface is critically corrupted after correcting for the average photometry of each SZA-similar area. Hence, residues coming from the heterogeneous photometry, as well as instrumental artifacts and atmospheric effects, may remain after the data pipeline.

Eventually, an region-of-interest (ROI) is defined as we are only interested in the southwest facing scarp displaying the defrosting features (see yellow line in Fig. 1). In addition, only the 250 CRISM channels ranging from 1.0 to 2.6 μm are considered due to the high impact of thermal noise for greater wavelengths and the less marked features of CO_2 ice in the visible range.

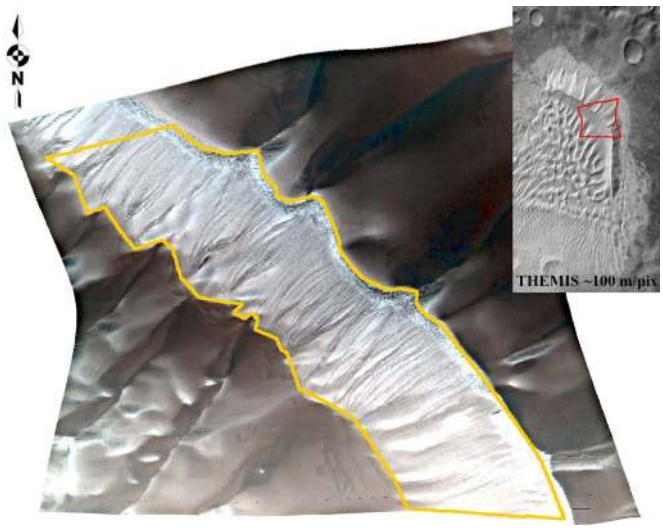

Fig. 1. CRISM frt000042aa true color image showing the Russell dune. The still-frosted scarp displays dark spots on the ridge of the dune and dark elongated patterns along the gullies. The region-of-interest (ROI) is highlighted in yellow. The upper right figure displays the location of the test image over the megadune observed by the THEMIS instrument.

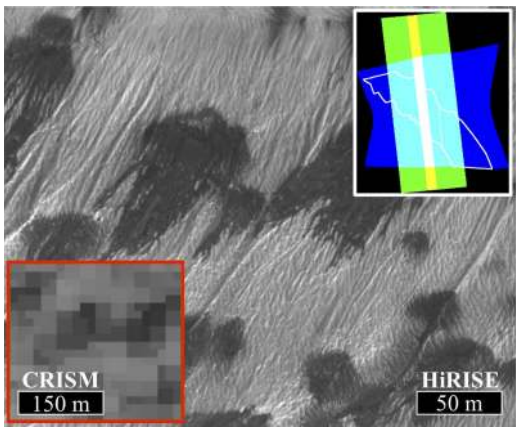

Fig. 2. Detail of the Russell dune observed by the CRISM and the HiRISE instruments. Upper right image: footprints of the images CRISM frt000042aa in blue (604 × 420 pixels, non-map projected), HiRISE PSP_002482_1255_RED in green (29 862 × 63 004 pixels, map projected), and HiRISE PSP_002482_1255_COLOR in yellow (11 776 × 61 257 pixels, map projected). The ROI is enclosed with a white line.

C. Building a Ground Truth

Although Mars is the planet other than Earth for which more data are available, the scarcity of ground truth to validate the statistical and physical algorithms that are used to retrieve information on the surface of the red planet is a crucial issue. On the one hand, only a few specific areas of Mars are enough characterized by a combined coverage of spacecrafts and rovers. Furthermore, both types of experiments provide information at very different spatial scales and thus confronting their results is a very challenging task. On the other hand, validation using simulated data generated from realistic surface and atmosphere models is not fully satisfactory due to the unavoidable limitations of the models. In this paper, a new strategy to validate the processing of planetary data is introduced. In particular, we propose the use of another type of imagery acquired over the Russell dune to build a ground truth for validation of spectral unmixing techniques.

1) HiRISE Data: The HiRISE camera is a unique tool to study the surface of Mars due to its very high spatial resolution. HiRISE consists of a half-meter reflecting telescope which allows taking three-channel (near-infrared, red, and blue-green) pictures with resolutions up to 25 cm/pix [31]. Two products are made available by HiRISE, a red-channel image making use of the full field of view and a three-channel image whose extent on the ground is significantly reduced.

Being aboard MRO, HiRISE is coordinated with CRISM to generate pair of images CRISM-HiRISE, displaying the same area of Mars. Fig. 2 (upper right) shows the footprints of the two products corresponding to the HiRISE image PSP_002482_1255 to be compared to the CRISM image frt000042aa. In this paper, the red-channel product is selected because of its larger coincident footprint as regards the CRISM image and twice better spatial resolution in comparison with the three-band image. Likewise, Fig. 2 shows the same area of the Russell dune observed by the CRISM and the HiRISE instruments. As it can be seen, HiRISE displays the dark features with a much greater detail, making them very distinguishable from the surrounding brighter ice. Hence, we propose to use the red-channel image PSP_002482_1255_RED to generate a reference abundance map corresponding to the dark features. The resulting ground truth will be then compared to the abundance maps obtained from the image frt000042aa, thus evaluating the performances of each unmixing technique in a similar and independent way.

The generation of the ground truth is as follows. First, the HiRISE image is classified by extracting the dark features. The resulting classification map and the CRISM image—previously projected onto the HiRISE geographic space—are registered by means of a feature matching method. Then, labels corresponding to the dark features are counted within the footprint of each CRISM pixel projected on the classification map. By doing this, the classification outcome is transformed into a reference abundance map against which the unmixing abundance maps will be compared in a pixel-wise manner.

2) Classification Map: The dark features are extracted by classifying the image PSP_002482_1255_RED into two classes, dark features and brighter ice, as suggested by geomorphologic analysis and the image histogram. With this aim, the image is split into k clusters according to gray value using a k-means strategy [32]. A value of $k = 7$ is satisfactory in our case. We note $\{L_1, \ldots, L_7\}$ the labels of the clusters and $\{C_1, \ldots, C_7\}$ their average values such that $(C_1 < \ldots < C_7)$. In order to represent the dark features, we select the darkest cluster L_1 which is manually improved by locally thresholding the original image. This operation takes into account the presence of shadows within the gullies that can be confused with elongated dark structures. Eventually, only the dark spots and the dark elongated features are classified as dark features while the rest of the image is classified as brighter ice. Fig. 3(a) shows the resulting classification map.

3) Image Registration: The classification map must be processed along with the CRISM image to allow an accurate pixel-wise comparison between the two final products (i.e., the ground truth coming from the HiRISE image and the abundance maps coming from the unmixing techniques). With this aim, we perform the registration of the HiRISE original image and the CRISM channel at 1.1 μm, which corresponds to the continuum of the spectra. One should note that the direct registration of the unmixing products is not reasonable since this might introduce some bias (e.g., if the unmixing results are wrong). The registration of CRISM and HiRISE images is very challenging because of the notable differences as regards the spatial resolution of both cameras ($\sim$72 times larger for HiRISE).

First, the selected CRISM channel is projected onto the HiRISE geographic space using the ancillary data of the image frt000042aa, which provide the latitude and longitude coordinates for each pixel. After this step, the two images are not correctly registered due to inaccuracies of pointing and limitations of the instrument models used to generate the geographical data of each sensor. That being so, we first perform a coarse registration of both images by applying a spatial translation whose Δl and Δc (where l and c stand for line and column, respectively) maximize the correlation coefficient between both images. Eventually, a Delaunay triangulation refines the registration by warping the CRISM image using a set of manually selected ground control points.

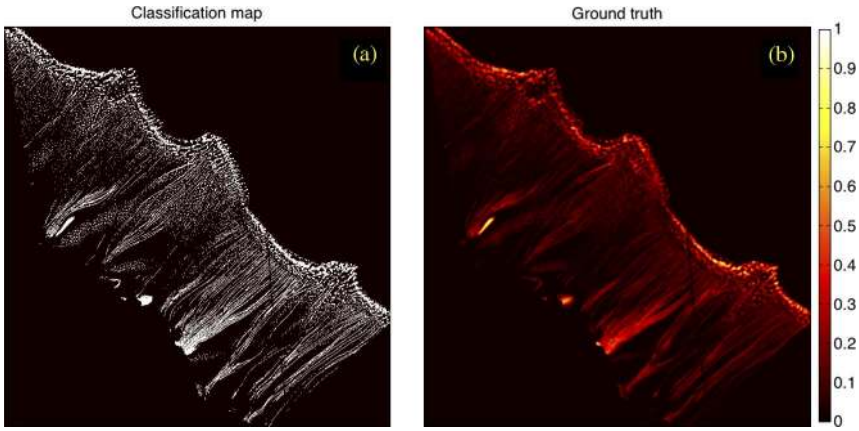

Fig. 3. (a) Classification map corresponding to the dark features extracted from the original HiRISE image. The label occurrences corresponding to the dark features are represented by white points. (b) Reference abundance map used as ground truth.

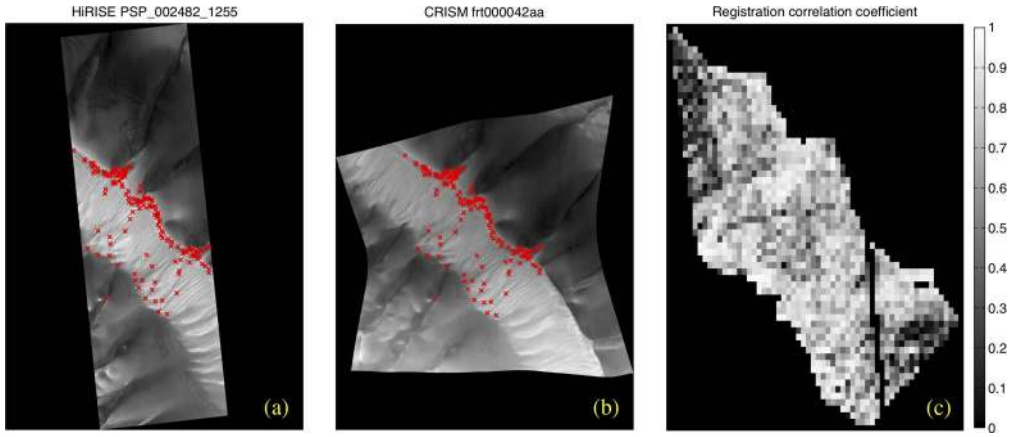

Fig. 4. (a) HiRISE image with the corresponding registration control points as red crosses. (b) The same as Fig. 4(a) for the CRISM image. (c) Registration accuracy map displaying the local correlation coefficient computed on the intersection between the two images and the ROI on a 10×10-pixel basis.

The registration step is detailed in Fig. 4. Fig. 4(a) and (b) show, respectively, the HiRISE and the CRISM images with the corresponding ground control points. More than 200 reference points are defined over the southwest-facing scarp, particularly for the dark spots along the ridge of the dune as they are critical features in the upcoming comparison. The accuracy of the registration is evaluated by calculating the local correlation coefficient r_{reg} between the HiRISE image and the CRISM channel at 1.1 μm after registration. Fig. 4(c) shows the ensemble of r_{reg} values that are obtained using a 10×10 sliding window over the area, resulting from the intersection of the two images and the ROI [see Fig. 2 (upper right)]. The resulting correlation map underlines the accuracy of the registration with an average correlation $r_{reg} = 0.7$. In addition, Fig. 4(c) provides valuable information on the distribution of the registration accuracy that will be used in the validation stage. Given the manual selection of control points and the size of the images ($29\,862 \times 63\,004$ pixels for the HiRISE image), misregistration inaccuracies affect this processing step, particularly on the borders of the processed area.

4) Reference Abundance Map: After registration, the HiRISE classification map is transformed into an abundance map. Since the data manipulation is performed on the HiRISE geographic space, each CRISM pixel is now associated to a footprint containing several pixels at the HiRISE resolution. That being so, the reference abundances are calculated by counting the number of dark labels occurring in each CRISM footprint. The result is then divided by the total number of labels. By doing this, we obtain an image that provides the abundance of dark features at the CRISM resolution.

One should note that the remotely sensed signal that determines the radiance value of each CRISM pixel comes not only from its conjugated area at the Martian surface (i.e., the theoretical footprint) but also the areas corresponding to the neighboring pixels. This additive contribution to the signal is originated by two principal causes. First, the spatial response of a single CRISM detector element—characterized by its Gaussian-shaped point spread function (PSF)—partially overlaps the PSFs of the neighboring detectors [1]. As a consequence, the final radiance value is the weighted sum of the contribution coming from the target pixel and its neighbors. In addition, CRISM images suffer from the so-called adjacency effect that is common to all 2-D imagers [33]. Due to the aerosol particles in the atmosphere, some photons coming from the neighboring area of a given pixel are scattered toward its corresponding detector element, thus contributing to the final radiance value. These two effects result in a blurring of the image that is not taken into account by the label counting process introduced previously. Since evaluating the coupling of the adjacency and PSF effects is not straightforward, the image blurring is mimicked

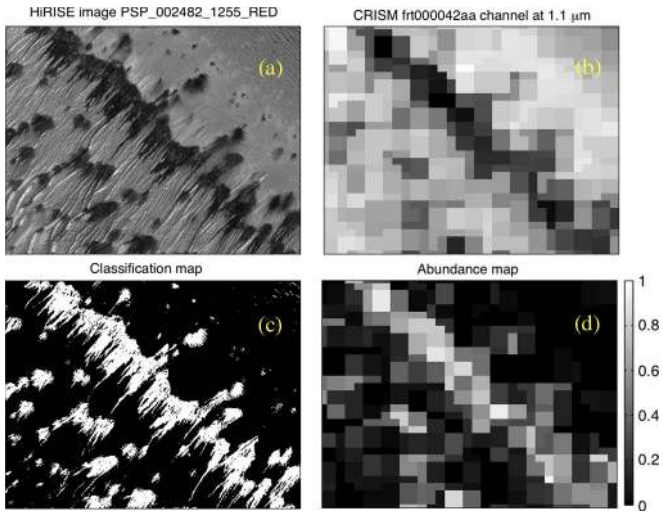

Fig. 5. Detail of the ground truth generation. (a), (b) HiRISE and CRISM images after registration. (c) Classification map highlighting the dark features. (d) Reference abundance map after pixel counting.

by filtering the reference abundance map by a Gaussian low-pass filter. The size of the Gaussian kernel is determined by optimizing the correlation coefficient between the registered CRISM channel at 1.1 μm and the filtered HiRISE image.

Fig. 3(b) shows the final ground truth that will be used for validating the unmixing products. Lastly, Fig. 5 illustrates the different processing steps on a small area of the Russell dune.

III. Spectral Unmixing

We note $\mathbf{X}$ the matrix representing the flatten hyperspectral image cube such that $\mathbf{X} = \{\mathbf{x}_1, \mathbf{x}_2, \ldots, \mathbf{x}_{N_p}\}$, where $\mathbf{x}_k = \{x_{1,k}, x_{2,k}, \ldots, x_{N_s,k}\}^T$. $x_{l,k}$ represents the value of the kth pixel at the lth channel, N_p is the number of pixels, and N_s is the number of spectral channels. We assume that the spectrum of each pixel can be reduced to a linear mixture of N_c endmember spectra, leading to the following instantaneous model:

$$\mathbf{X} = \mathbf{M} \cdot \mathbf{S} + \mathbf{e} \tag{1}$$

where $\mathbf{e}$ stands for the additive noise in the image, $\mathbf{M} = \{\mathbf{m}_1, \mathbf{m}_2, \ldots, \mathbf{m}_{N_c}\}$ is the mixing matrix, being $\mathbf{m}_n$ the spectral signature—the characteristic spectrum—of the nth endmember, and $\mathbf{S} = \{\mathbf{s}_1, \mathbf{s}_2, \ldots, \mathbf{s}_{N_c}\}^T$ is the source matrix with $\mathbf{s}_n = \{s_{n,1}, s_{n,2}, \ldots, s_{n,N_p}\}$. $s_{n,k}$ correspond to the abundance of the nth endmember at the kth pixel and its positivity is generally imposed. Besides, the endmember abundances must respect the sum-to-one constraint such that $\sum_{n=1}^{Nc} s_{n,k} = 1, \forall k$. In order to extract $\mathbf{M}$ and $\mathbf{S}$ from $\mathbf{X}$ without any *a priori* information, N_c must be estimated in the first place. An endmember extraction approach is then applied to retrieve $\mathbf{M}$, followed by the reconstruction of $\mathbf{S}$ based on the extracted spectra and the linear model of (1).

Physical assumptions leading to the linearity of the remote sensing signal are enumerated in [12] as: (i) predominance of linear subpixel mixing at the ground; (ii) absence of nonlinear mixing; (iii) Lambertian surface or homogeneity of surface illumination conditions; and (iv) absence of atmospheric absorption and scattering. In this paper, the presence of linear subpixel mixing in some specific areas of the Russell dune has been demonstrated by the scrutiny of the HiRISE image in Section II-C-1. Due to the lower spatial resolution of the CRISM instrument, the hyperspectral signal corresponding to some specific areas is composed by the signatures of two physically distinct components at the surface, resulting in geographic subpixel mixtures. By contrast, the absence of nonlinear mixtures cannot be assured as that would require data at the grain-size scale. A first attempt to address this point is presented in Section V by relating the reconstruction error of the spectra to the existence of nonlinearities. Future work will further expand this issue by performing a complete physical analysis of the test image as it is stated in Section VI. As regards atmospheric contributions, assumptions of linearity are met after the preprocessing in Section II-B-1. However, potential residues may lead to perturbations on the spectral unmixing process. Likewise, the heterogeneity of surface illumination may also result in some artifacts. All the previous factors $\mathbf{F} = \{\mathbf{f}_1, \mathbf{f}_2, \ldots, \mathbf{f}_{N_c}\}$, including residues coming from instrumental artifacts, may transform the linear mixing assumption into the degenerated model

$$\mathbf{X} = \Im(\mathbf{M} \cdot \mathbf{S}) + \mathbf{e} \simeq \mathbf{F} \cdot \mathbf{M} \cdot \mathbf{S} + \mathbf{e} \tag{2}$$

where $\Im(X) = \mathbf{F} \cdot X + \mathbf{F}_2 \cdot X^2 + \ldots \simeq \mathbf{F} \cdot X$. Furthermore, spurious transformations arising from $\mathbf{F}$ may affect the physical sources $\mathbf{M}$. In that case, the number of endmembers estimated by the following methods may become higher for $\mathbf{F} \cdot \mathbf{M} \cdot \mathbf{S}$ than it is for $\mathbf{M} \cdot \mathbf{S}$.

A. Estimation of the Number of Endmembers

Two methods are considered in order to estimate the number of endmembers in the image frt000042aa, the widely used Hyperspectral Signal Subspace Identification by Minimum Error (HySIME) approach and the recent Eigenvalue Likelihood Maximization (ELM) technique, which has been originally developed for hyperspectral data from Mars.

1) HySIME*:* This approach has been recently proposed as a minimum mean square error-based approach to infer the signal subspace in hyperspectral imagery [34]. HySIME is eigendecomposition-based, unsupervised, and fully automatic. It first estimates the signal and noise correlation matrices and then selects the subset of eigenvalues that best represents the signal subspace in the least squared error sense. The performances of HySIME have been validated satisfactorily by using simulated and terrestrial remotely sensed hyperspectral data.

2) ELM: This technique is proposed as an automatic and unsupervised algorithm for estimating the number of endmembers of hyperspectral images [14]. This approach is based on the distribution of the eigenvalues corresponding to the correlation and covariance matrices of $\mathbf{X}$. In particular, ELM assumes that the couple of nth eigenvalues of both matrices correspond to the variance of the noise for $n > N_c$. That being so, the distribution of the difference between a couple of eigenvalues z_n is asymptotically modeled by a Gaussian probability density function centered at zero for $n > N_c$ and a non-zero value otherwise. Based on this property, ELM builds a likelihood function depending on z_n that shows a global maximum for

$n = N_c$. In [14], this approach is validated using simulated data and hyperspectral images from Mars acquired by the OMEGA instrument. However, ELM supposes the Gaussianity of the noise while CRISM noise is hardly Gaussian.

B. Endmember Extraction

After estimating the number of endmembers N_c of the test image, we perform a selection of state-of-the-art algorithms based on different principles as follows: (i) geometric techniques assuming the presence of pure pixels in the image; (ii) geometric approaches without pure pixel assumption; and (iii) statistic methods based on a Bayesian framework. In addition, we consider the incorporation of spatial information by performing spatial preprocessing on the image frt000042aa. The endmember extraction techniques considered in this paper are briefly explained as follow.

1) VCA: VCA has been proposed as an efficient and fast geometric method for extracting endmembers under a linear mixing supposition [13]. According to the sum-to-one condition, the data vectors $\mathbf{x}_k$ are always inside a simplex formed by $\mathbf{M} \cdot \mathbf{S}$ whose vertex are the spectra of the endmembers. VCA iteratively projects the data onto the orthogonal direction to the subspace spanned by the already extracted endmembers, designating the most extreme projection as the next endmember. The process is repeated until N_c endmembers are found. That being so, VCA assumes that (i) there are pure pixels in the data and (ii) there is no noise. However, the latter means that $\mathbf{x}_k$ may be outside the simplex if noise is present. In [14], VCA is evaluated satisfactorily on OMEGA data from Mars and therefore it may be suitable for spectral unmixing of CRISM data.

2) N-FINDR: The widely used N-FINDR algorithm extracts extreme points of the simplex of maximum volume that can be inscribed within $\mathbf{X}$ using a simple nonlinear inversion [15]. This approach iteratively selects random endmembers and evaluates whether the volume of the simplex sustained by those endmembers changes or not. The convex nature of hyperspectral data allows this operation to be performed in a quick and relatively straightforward manner. Contrarily to VCA, N-FINDR is a truly simplex volume-based technique. However, this method may become less efficient and not reproducible due to its randomness. N-FINDR has been applied on CRISM data with satisfactory results in [16].

3) MVC-NMF: This technique is proposed for endmember extraction of highly mixed hyperspectral data without the pure pixel assumption [17]. MVC-NMF decomposes mixed pixels by analyzing the connection between the spectral unmixing analysis and the non-negative matrix factorization. A minimum volume constraint makes the MVC-NMF learning less dependent on the initializations, robust to different levels of noise, less sensitive to the estimated number of endmembers, and applicable to images with or without pure pixel representations. Experiments in [17] indicate that MVC-NMF has the potential of identifying less prevalent endmembers and thus it may be suitable for extracting the dark features in frt000042aa.

4) MVES: The recent MVES approach proposes a convex analysis without involving pure pixels [18]. Through an affine set fitting of observed pixels followed by the use of Craig's unmixing criterion, the MVES problem aims at minimizing a simplex volume subject to the constraint that all the dimension-reduced pixels are enclosed in the simplex. MVES utilizes linear programs to approximate the unmixing problem in a cyclic fashion. MVES might be suitable for this paper since it has proved to work well for endmembers with low purity levels and to outperform the VCA and MVC-NMF algorithms [18].

5) SISAL: Recently, the SISAL method has been proposed to solve the linear unmixing of the minimum volume simplex without pure pixel assumption [19]. Being a non-convex optimization problem with convex constraints, the positivity constraints are replaced by soft constraints, forcing the spectral vectors to belong to the convex hull of the endmember signatures. The resulting problem is solved by a sequence of augmented Lagrangian optimizations. SISAL may be appropriate for the unmixing of the test image due to its effectiveness. In [19], SISAL is satisfactorily validated on simulated data through comparison to other state-of-the-art methods such as VCA and MVES.

6) BPSS: This algorithm proposes to estimate the matrices $\mathbf{M}$ and $\mathbf{S}$ in a Bayesian framework under a linear model with inherent positivity and additivity constraints and no pure pixel assumption [35]. In BPSS, the noise $\mathbf{S}$ and $\mathbf{M}$ are assumed to follow a Gaussian, Dirichlet, and Gamma probability density functions, respectively. BPSS is based on hierarchical Bayesian models to encode prior information regarding the parameters of interest. The complexity of the estimation from the resulting posterior distribution is overcome using Markov chain Monte Carlo methods. In BPSS, the degree of uncertainty affecting the extracted endmember spectra can be estimated since results are computed as probability distribution functions. In [36], numerical schemes are devised to reduce the computation time which is a critical point of BPSS. This method has been applied satisfactorily on OMEGA hyperspectral images in [12] yet never on CRISM's.

7) Spatial Preprocessing: The authors of [21] propose a preprocessing to incorporate spatial information into the unmixing of hyperspectral images. For each pixel, a scalar factor related to the spectral similarity of spectra lying within a certain spatial neighborhood—determined by the window size w_s—is estimated. This value is then used to weigh the importance of the spectral information associated to each spectrum in terms of its spatial context. After applying a traditional endmember extraction technique on the preprocessed image, the spatial position of each endmember is retrieved. Then, the reconstruction of the abundance maps is carried out by using the analogous spectra from the original image and a linear mixture model. This preprocessing enhances the search for endmembers in spatially homogeneous areas while it may penalize the detection of anomalous sources. This Preprocessing can be combined only with methods such as VCA and N-FINDR, as the existence of pure pixels is required to retrieve the position of the endmembers in the preprocessed image.

IV. Experiments

Experiments are conducted on the preprocessed image frt000042aa. We recall that only the spectra encompassed by

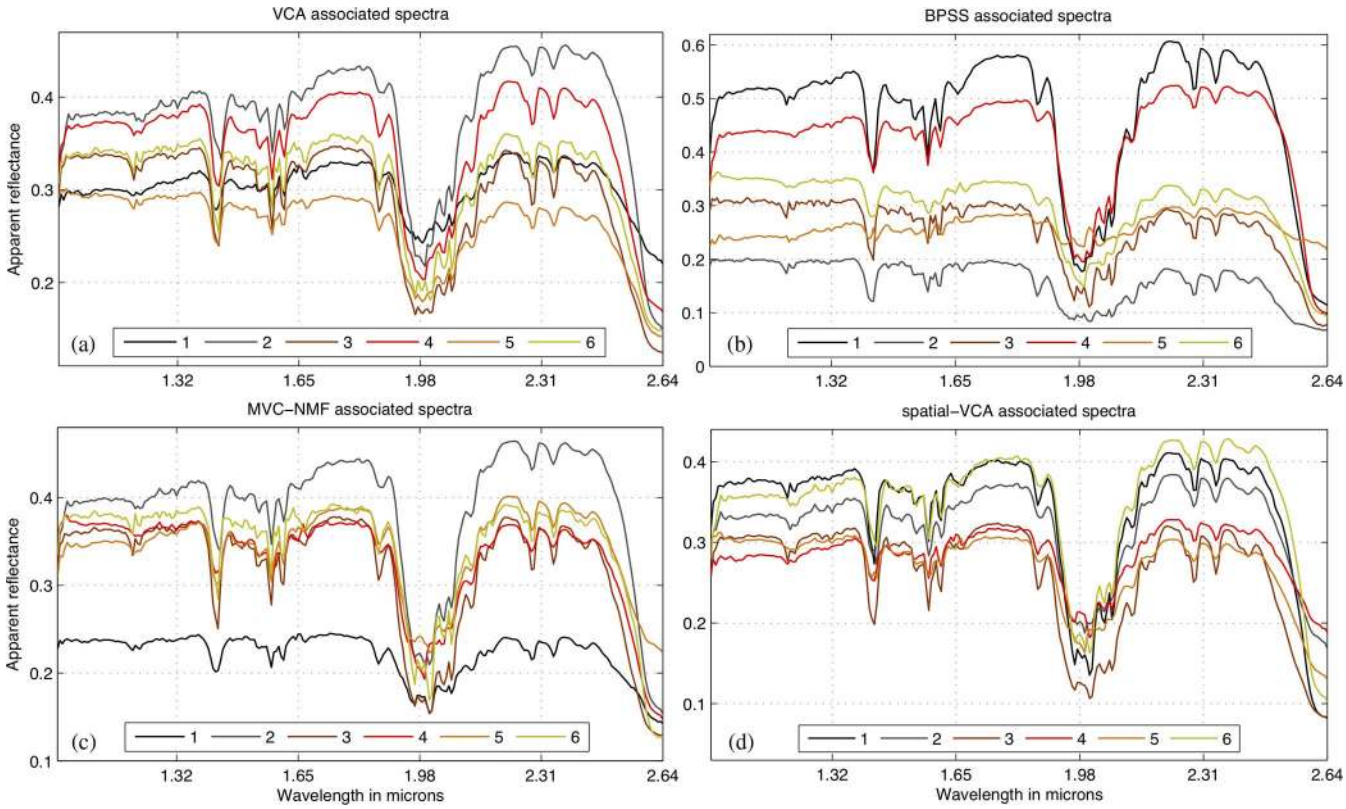

Fig. 6. Extracted spectra by the (a) VCA, (b) BPSS, (c) MVC-NMF, and (d) spatial-VCA methods.

the defined ROI are considered. By performing spectral unmixing, we consider two main objectives, (i) the extraction of physically meaningful sources and their corresponding distribution maps that help understanding the physical state of the Russell dune and (ii) the obtention of a physical source related to the dark features to be compared to the ground truth generated in Section II-C. One should note that while the achievement of the second purpose is not mandatory (yet desirable), the first objective is crucial for the validation of spectral unmixing techniques in a planetary context.

First, the number of endmembers in the image frt000042aa is determined by the two methods presented in Section III-A. On one hand, the HySIME technique determines $N_c = 14$. Given that the Russell dune is assumed to be composed by two components—CO_2 ice and dust—this result largely exceeds the expected number of sources in the image. Furthermore, the analysis of 14 extracted endmembers turns into a rather unfeasible task. The reason of this result may come from a higher sensitivity of HySIME to subtle contributions in the image that could be valuable in other situations out of the scope of this paper such as the detection of residual artifacts. Therefore, HySIME is not further considered in this paper. On the other hand, the ELM technique detects the presence of six endmembers. This result seems to correspond more satisfactorily to the physical scenario prevailing in the Russell dune and corroborates the good performances of ELM when applied to OMEGA hyperspectral data from Mars [14]. As regards the requirement of Gaussian noise by ELM, the VCA endmember extraction was conducted with $N_c = \{4 \ \ldots \ 8\}$ in order to evaluate the robustness of the N_c estimation by ELM. However, experiments with $N_c \neq 6$ did not provide any significant improvement regarding the unveiling of the physical sources. For this reason and since a similar conclusion would be likely drawn from operating the other methods in the same way, all the presented experiments are carried out by using $N_c = 6$.

As regards endmember extraction, all the techniques introduced in Section III-B are applied on the test image. However, the results of a few methods are not shown in this paper, as they do not meet the main objectives detailed above. For example, MVES and SISAL are not further considered as they both extract an endmember whose associated spectrum cannot be explained from a physical point of view. This is in agreement with the fact that both methods are based on simplex volume optimization and therefore may extract endmembers absent in the image. Although MVC-NMF and BPSS do not consider the pure pixel assumption either, they provide satisfactory endmembers and therefore are considered in this paper. Likewise, the results of the N-FINDR algorithm are not shown in this section since a satisfactory source related to the dark features could not be extracted, contrarily to VCA. As a consequence, the spatial preprocessing introduced in Section III-B7 is exclusively combined with the VCA approach, thus defining the method referred to as spatial-VCA. The window size w_s is set equal to five as it is recommended in [21] and given that larger values may affect the endmembers related to the spatially confined dark features. Hence, in this paper, we present the experimental results of performing spectral unmixing of the image frt000042aa by the following endmember extraction methods based on different principles: (i) the VCA method with assumption of pure pixels; (ii) the BPSS technique based on

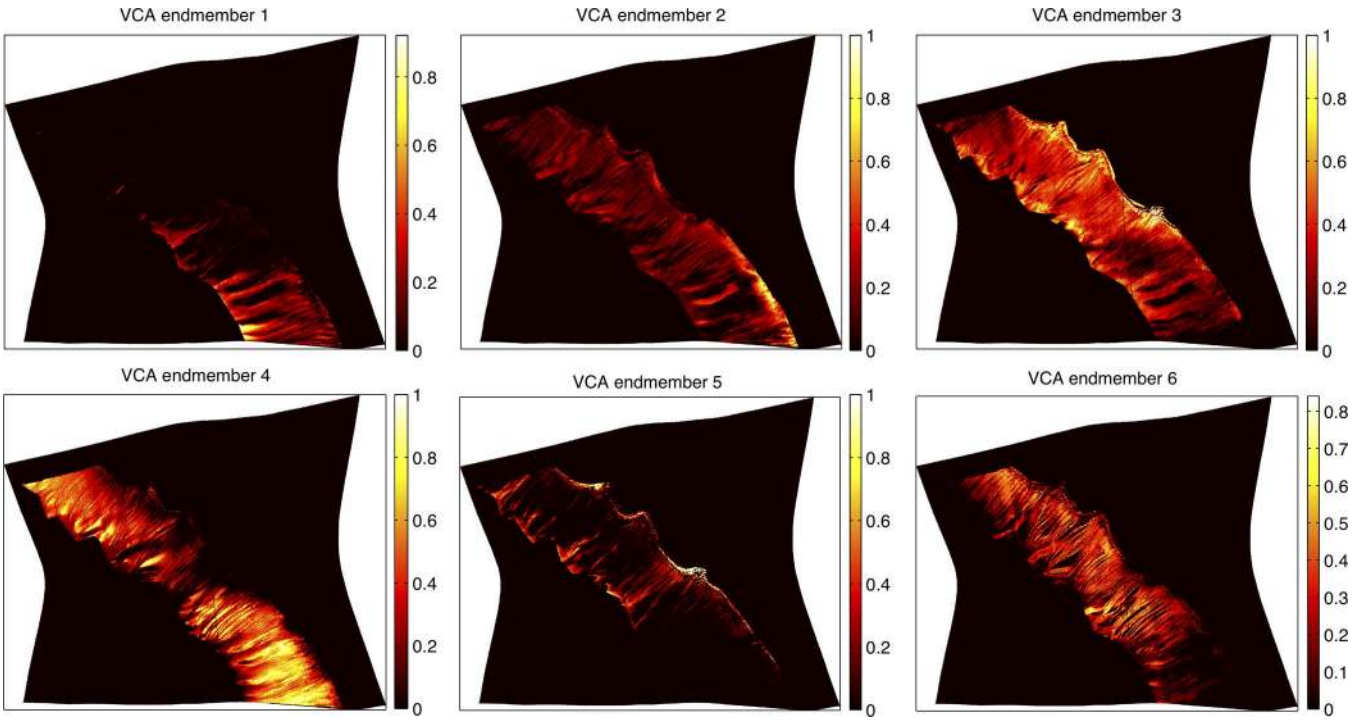

Fig. 7. Abundance maps corresponding to the six endmembers extracted using VCA.

a Bayesian framework; (iii) the MVC-NMF approach with no assumption of pure pixels; and (iv) the spatial-VCA algorithm that incorporates the existent spatial information in the image. As for the reconstruction of the abundance maps using the linear mixing model, the non-negativity and the sum-to-one constraints are considered for all methods.

A. General Interpretation

The spectra corresponding to the six endmembers extracted by each method are plotted in Fig. 6. Then, Figs. 7–10 show the associated abundance maps. Based on the information coming from both products, a similar physical interpretation of the scene is performed independently for each method, leading to the definition of three physical sources. Due to residual artifacts and other nonlinearities, the spectral unmixing of the image frt000042aa is affected by source splitting effects (see Section III), thus making necessary the recombination of the six endmembers into three physical sources. After assigning each extracted endmember to one of the three physical sources, the abundance map of a given physical source is obtained by adding the individual abundances of the associated endmembers. The results of this recombination are shown in Fig. 11. The robustness of the proposed interpretation is underlined by the notable similarities among the physical sources that are reconstructed for each method.

In order to identify the origin of each endmember, two parameters are defined from each extracted spectrum. Let $R_{1.1}$ be the apparent reflectance value at 1.1 μm and let $B_{2.3}$ be the absorption depth at 2.3 μm such that $B_{2.3} = 1 - R_{2.3}/R_{2.2}$. These two spectral parameters are decisive for the interpretation of the endmembers together with the information coming from the abundance maps. In particular, large values of $R_{1.1}$ and $B_{2.3}$ are related to a higher content of CO_2 ice because of its higher reflectance in comparison to dust and the fact that absorption at 2.3 μm is specific to ice, respectively. Due to inaccuracies in the atmospheric correction (see Section II-B-1), extracted spectra may have an anomalous positive or negative slope that must be accounted for the calculation of $B_{2.3}$. With this aim, we multiply $B_{2.3}$ by the spectrum average slope $b_{1.1-2.2}$ that is calculated as $R_{2.2}/R_{1.1}$. Tables I–IV detail the previous parameters for each endmember extracted with VCA, BPSS, MVC-NMF, and spatial-VCA, respectively.

The three physical sources that are defined based on the unmixing results are briefly described by detailing their spectral and spatial characteristics. The physical interpretation of each source is kept to a minimum since it is not the aim of this paper.

- Dark source: physical source related to the presence of dark features. The corresponding $R_{1.1}$ and $B_{2.3}$ are the lowest among the three sources due to a high content in dust and a few residual CO_2 ice. This source predominates along the ridge of the dune and within the gullies in the form of dark spots and elongated patterns, respectively.
- Strong bright source: physical source related to a high content of CO_2 ice. The corresponding $B_{2.3}$ is the highest among the three sources while $R_{1.1}$ is higher than for the dark source due to a lower dust content. This source predominates principally in the areas surrounding the dark source.
- Weak bright source: physical source related to a high content of CO_2 ice. The corresponding $R_{1.1}$ is the highest among the three sources while $B_{2.3}$ is higher than for the dark source but lower than for the strong bright source. This source may correspond to a physical state of the ice—different from the strong bright source—that greatly predominates on the dune scarp.

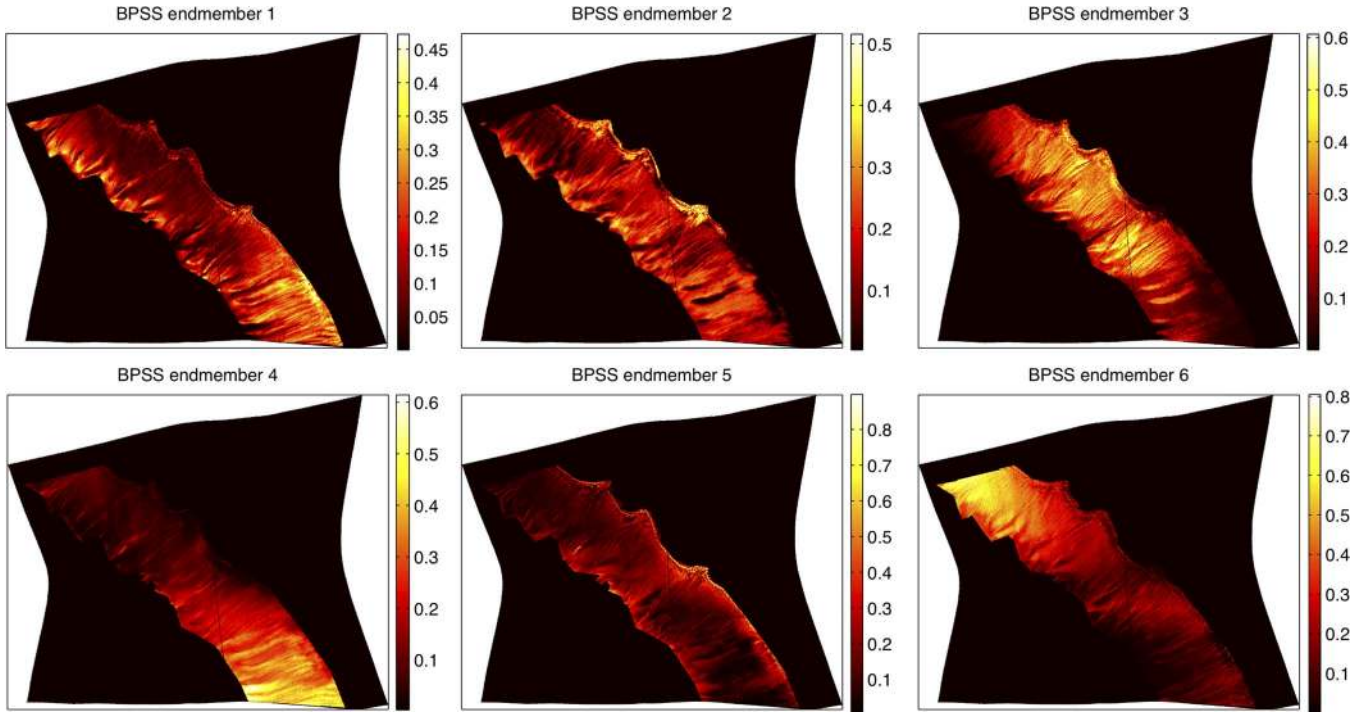

Fig. 8. Abundance maps corresponding to the six endmembers extracted using BPSS.

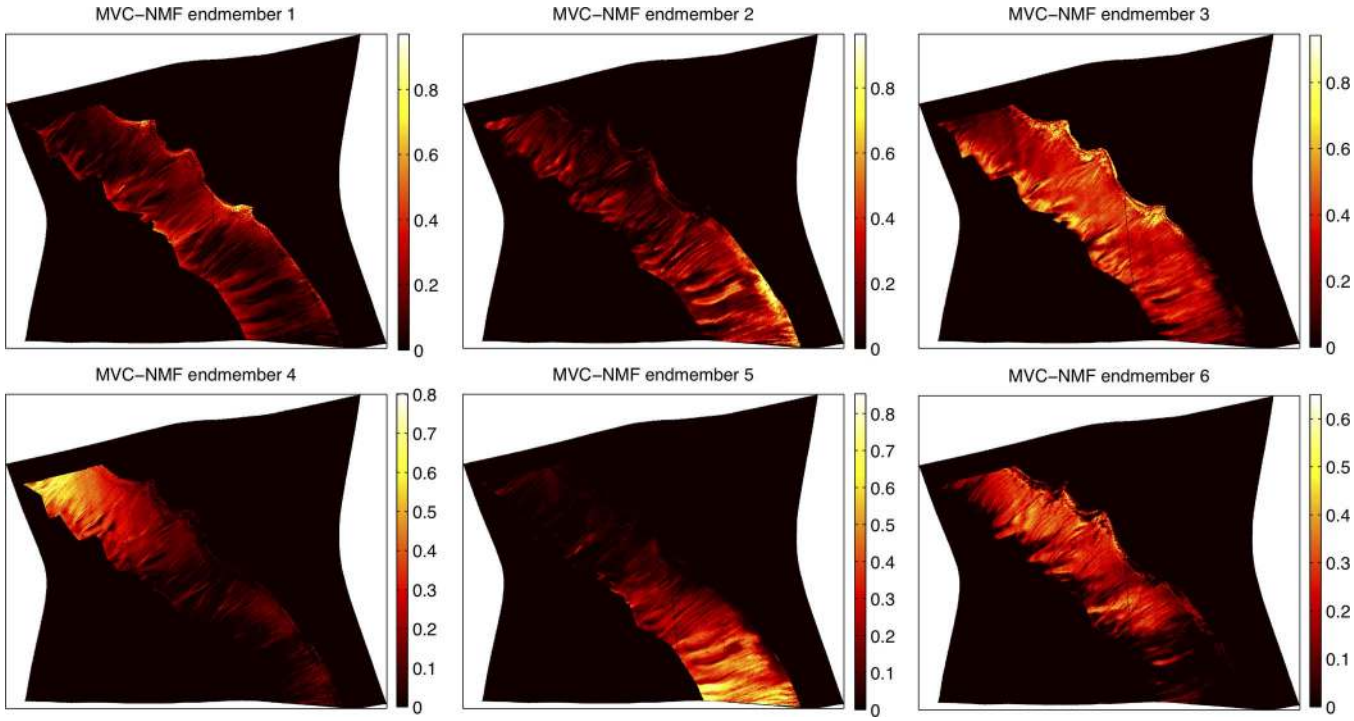

Fig. 9. Abundance maps corresponding to the six endmembers extracted using MVC-NMF.

In the following sections we detail, for each method, the recombination process that is carried out to reconstruct the three physical sources.

B. VCA

The interpretation of the endmembers extracted by VCA is conducted by examining the associated spectra and abundance maps in Figs. 6(a) and 7, respectively. The spectral parameters $R_{1.1}$ and $B_{2.3}$ are detailed in Table I. Lastly, the recombined abundance maps corresponding to the physical sources are displayed in Fig. 11(a).

1) Dark Source: Endmembers 1 and 5 are identified to be related to the dark source due to the lowest $R_{1.1}$ and $B_{2.3}$ among the six endmembers.

The combination of the two endmembers into a single physical source is also justified by the opposite vertical trends that affect the abundance maps 1 and 5. Both maps show

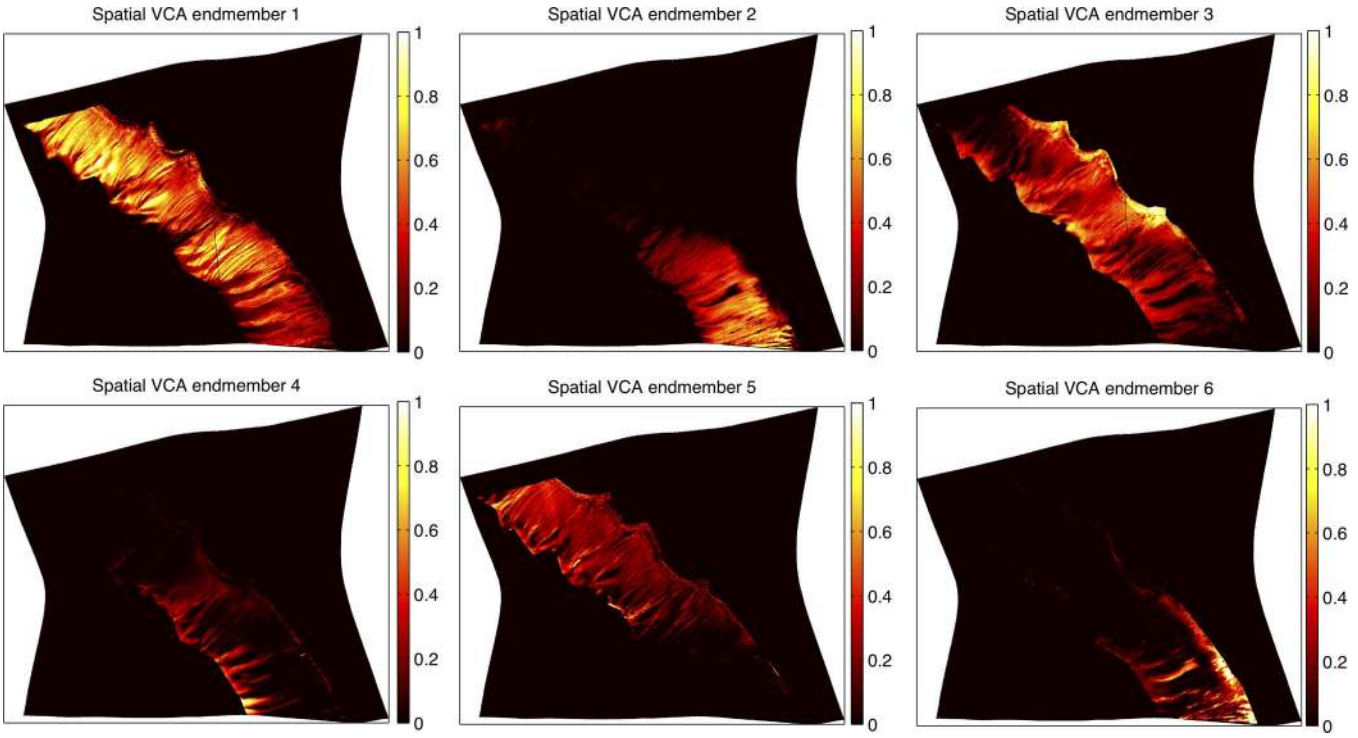

Fig. 10. Abundance maps corresponding to the six endmembers extracted using spatial-VCA.

very low spurious abundances, either for the top or the bottom rows, coming from the atmospheric residue described in Section II-B-1. This interpretation is also pointed out by the complementary slopes of the spectra ($b_{1.1-2.2} > 1$ for endmember 1 and $b_{1.1-2.2} < 1$ for endmember 5).

The abundance map resulting from the fusion of the two initial abundance maps eliminates the vertical trend, thus revealing the dark structures over the Russell dune. As a matter of fact, the red pixels of the recombined abundance map highlight the dark spots on the top of the dune, the dark elongated patterns along the gullies and some areas belonging to the base of the northeast-facing defrosted scarp.

2) Strong Bright Source: Endmember 3 is identified to represent the strong bright source due to the highest $B_{2.3}$ among all the extracted endmembers and a medium $R_{1.1}$.

The abundance map of the strong bright source shows a spatial coherence with the dark source as the green areas surround the red pixels, particularly on the top of the dune.

3) Weak Bright Source: Endmembers 2, 4, and 6 are identified as being related to the weak bright source as they all correspond to the highest $R_{1.1}$ and a medium $B_{2.3}$.

The splitting phenomenon that affects this physical source comes from the coupling of two nonlinear residues. On the one hand, the predominance of CO_2 ice for this physical source leads to a typical smile pattern in the abundance map of endmember 6 (see Section II-B-1). This is pointed out by the anomalous lower abundances for the horizontal edges. The presence of a spectral smile residue makes endmember 6 enough energetic to be extracted independently. On the other hand, the differences of $R_{1.1}$ among the three endmembers are explained by the different illumination conditions that happen over the scene. A qualitative study of the HiRISE DTM corresponding to the Russell dune (see Section II-B-1) reveals that endmember 6 predominates at low SZA while endmembers 2 and 4 correspond to SZA values that are similar to the average angle used in the photometric correction. An accurate photometric correction by the real SZA would increase $R_{1.1}$ for endmember 6, thus matching the other two endmembers in terms of apparent reflectance.

The abundance map resulting from the fusion of the three endmembers highlights in blue the areas which are poor in dark and strong bright sources.

C. BPSS

Given the nature of the BPSS algorithm the interpretation of the corresponding results must be carried out differently than it is done for VCA. As it is stated in Section III-B, BPSS may extract associated spectra that do not exist in the hyperspectral image. As a consequence, the parameters $R_{1.1}$ and $B_{2.3}$, shown in Table II, are less relevant and must be taken into account in an indicative manner. Similarly to VCA, Figs. 6(b), 8, and 11(b) detail the results of BPSS.

1) Dark Source: Endmember 5 is identified to be related to the dark features according to the lowest $B_{2.3}$. While having the lowest $R_{1.1}$, endmember 2 is not interpreted as representing the dark source since such a low level of apparent reflectance does not exist in the image and is unphysical (see Section IV-C2 for more details).

Besides the agreement of the extracted spectrum with the characteristic spectral features of the dark source, the abundance map of endmember 5 is correlated with the dark structures revealed by the other methods.

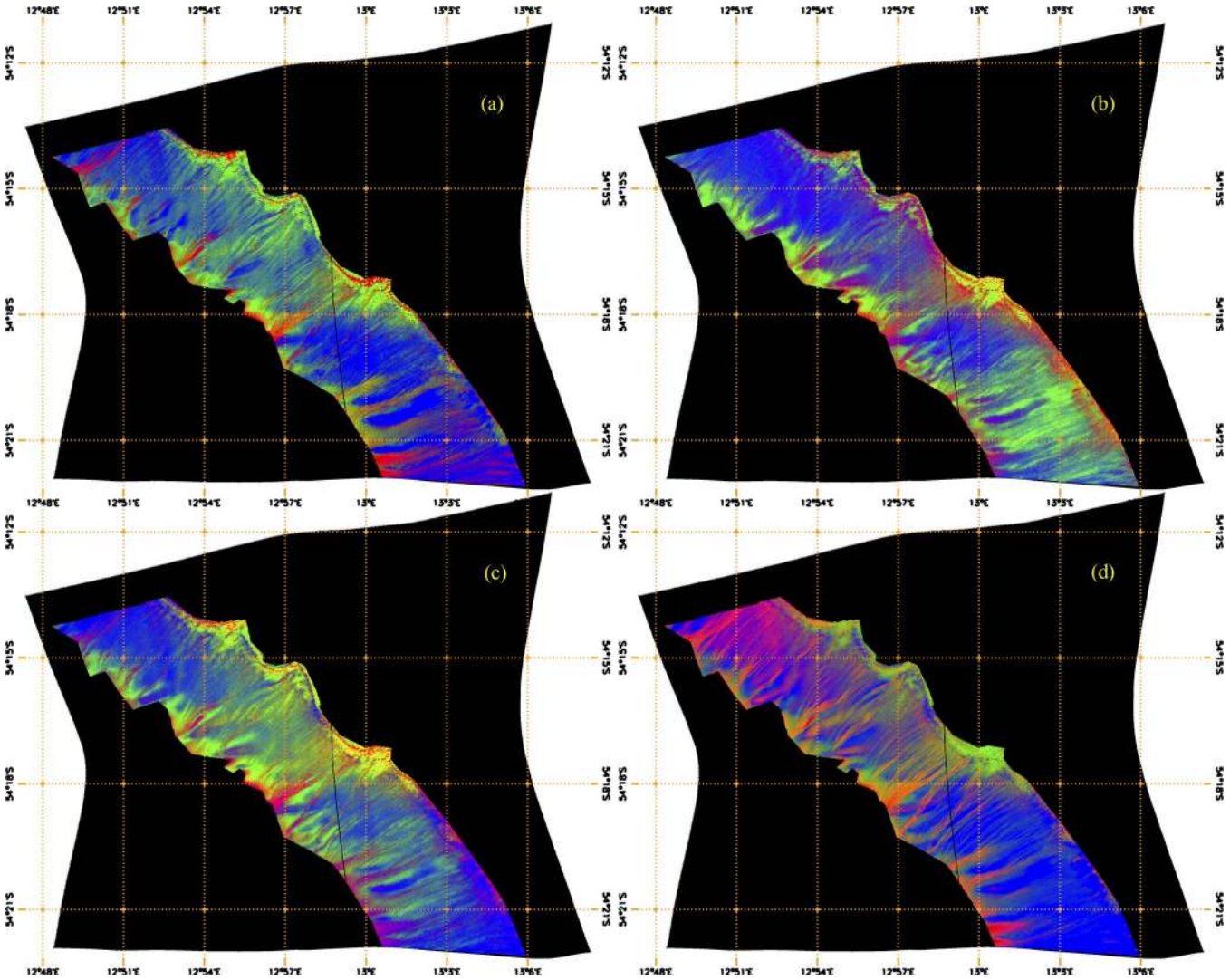

Fig. 11. (a) Color composite image illustrating the spatial distribution of the three physical sources over the Russell dune extracted by VCA. The dark, strong bright, and weak bright sources are show in red, green, and blue, respectively. (b), (c) and (d) Same as Fig. 11(a) for BPSS, MVC-NMF, and spatial-VCA.

TABLE I
VCA ENDMEMBERS—APPARENT REFLECTANCE AT 1.1 μm AND ABSORPTION DEPTH AT 2.3 μm—(D): DARK SOURCE, (S): STRONG BRIGHT SOURCE, (W): WEAK BRIGHT SOURCE

Endmember:	1 (D)	2 (W)	3 (S)	4 (W)	5 (D)	6 (W)
$R_{1.1}$:	**0.29**	**0.38**	**0.34**	**0.37**	**0.29**	**0.35**
$b_{1.1-2.2}$:	1.15	1.20	1.02	1.13	0.98	1.06
$B_{2.3}$:	**0.07**	**0.10**	**0.17**	**0.12**	**0.09**	**0.13**

TABLE II
BPSS ENDMEMBERS—APPARENT REFLECTANCE AT 1.1 μm AND ABSORPTION DEPTH AT 2.3 μm—(D): DARK SOURCE, (S): STRONG BRIGHT SOURCE, (W): WEAK BRIGHT SOURCE

Endmember:	1 (S)	2 (S)	3 (W)	4 (W)	5 (D)	6 (W)
$R_{1.1}$:	**0.51**	**0.20**	**0.31**	**0.43**	**0.24**	**0.35**
$b_{1.1-2.2}$:	1.18	0.91	0.95	1.20	1.25	0.96
$B_{2.3}$:	**0.15**	**0.25**	**0.17**	**0.09**	**0.08**	**0.11**

TABLE III
MVC-NMF ENDMEMBERS—APPARENT REFLECTANCE AT 1.1 μm AND ABSORPTION DEPTH AT 2.3 μm—(D): DARK SOURCE, (S): STRONG BRIGHT SOURCE, (W): WEAK BRIGHT SOURCE

Endmember:	1 (D)	2 (W)	3 (S)	4 (W)	5 (W)	6 (W)
$R_{1.1}$:	**0.24**	**0.39**	**0.36**	**0.37**	**0.34**	**0.38**
$b_{1.1-2.2}$:	1.01	1.17	1.04	1.00	1.16	1.03
$B_{2.3}$:	**0.08**	**0.08**	**0.16**	**0.08**	**0.10**	**0.10**

TABLE IV
spatial-VCA ENDMEMBERS—APPARENT REFLECTANCE AT 1.1 μm AND ABSORPTION DEPTH AT 2.3 μm—(D): DARK SOURCE, (S): STRONG BRIGHT SOURCE, (W): WEAK BRIGHT SOURCE

Endmember:	1 (W)	2 (W)	3 (S)	4 (D)	5 (D)	6 (W)
$R_{1.1}$:	**0.37**	**0.33**	**0.30**	**0.28**	**0.29**	**0.36**
$b_{1.1-2.2}$:	1.10	1.16	1.04	1.18	0.97	1.20
$B_{2.3}$:	**0.11**	**0.11**	**0.21**	**0.09**	**0.09**	**0.10**

2) Strong Bright Source: Endmembers 1 and 2 are related to the strong bright source. Due to the combination of the atmospheric residue and the BPSS properties, this source has been split into two endmembers that do not exist in the image and are difficult to explain from a physical point of view. The combination of both endmembers is necessary to obtain

a coherent strong bright source in terms of spectrum and abundance map. This interpretation is justified by the following reasons based on the examination of the associated spectra: (i) The spectral slope of both spectra is complementary due to the atmospheric residue as in Section IV-B1 ($b_{1.1-2.2} > 1$ for endmember 1 and $b_{1.1-2.2} < 1$ for endmember 2); (ii) a spurious fingerprint at 2 μm for endmember 1, which is reversed for endmember 2; and (iii) the $R_{1.1}$ values of both endmembers are either too high or too low from a physical point of view. Likewise, the abundance maps also confirm this interpretation since (i) the endmembers 1 and 2 show a strong anticorrelation (for all k pixels with $s_{1,k} + s_{2,k} > 50\%$, $correlation(s_{1,k}, s_{2,k}) = -0.62$) and (ii) endmembers 1 and 2 are always present in similar proportions (for all k pixels with $s_{1,k} + s_{2,k} > 50\%$, $mean(s_{1,k}) = 0.26$, $var(s_{1,k}) = 3.10^{-3}$, $mean(s_{2,k}) = 0.30$, $var(s_{2,k}) = 4.10^{-3}$). It is straightforward to verify that the combination of these two endmembers using similar proportions results in a spectrum with similar $R_{1.1}$ and $B_{2.3}$ to the strong bright source extracted by the other methods.

Similarly to VCA, the resulting abundance map of the strong bright source shows a strong correlation with those areas surrounding the dark source pixels. In addition, several yellow pixels coming from the combination of the dark and strong bright sources are observed over the dune ridge. This is in agreement with a linear mixing scenario for which the spatial resolution of CRISM may not suffice to resolve both sources.

3) Weak Bright Source: The weak bright source is composed by endmembers 3, 4, and 6. The associated spectra of endmembers 4 and 6 correspond to a high $R_{1.1}$ and medium $B_{2.3}$. Again, the spectrum of endmember 3 presents a $R_{1.1}$ and $B_{2.3}$ that cannot be found in the image.

Similarly to the VCA dark source, endmembers 4 and 6 show strong values at the bottom or the top of the image. This anomaly is originated in the atmospheric residue as the slopes of the two endmembers underline ($b_{1.1-2.2} > 1$ for endmember 4 and $b_{1.1-2.2} < 1$ for endmember 6). Contrarily, endmember 3 is particularly dominant in the center of the image with abundance values up to 0.6, indicating an origin linked with the smile effect residue (see Section IV-B3).

The regions corresponding to the weak bright source are widespread over the dune scarp as shown by the combined abundance map.

D. MVC-NMF

The examination of the endmembers extracted by the MVC-NMF algorithm are conducted by examining the associated spectra and abundance maps shown in Figs. 6(c) and 9, respectively. The corresponding spectral parameters $R_{1.1}$ and $B_{2.3}$ are detailed in Table III while the combined abundance maps corresponding to the physical sources are displayed in Fig. 11(c). Similarly to BPSS, MVC-NMF may extract spectra that are absent from the image and thus the spectral parameters must be considered carefully.

1) Dark Source: Endmember 1 is identified as the dark source due to the lowest $R_{1.1}$ among all endmembers. Contrary to VCA and BPSS, the parameter $B_{2.3}$ is less discriminative for MVC-NMF as all spectra, except for number 3, have similar low values.

Again, the corresponding abundance map reveals the structures related to the dark features with high accuracy.

2) Strong Bright Source: Endmember 3 is identified to be related to the strong bright source due to the highest $B_{2.3}$ among all the extracted endmembers.

Similarly to the other methods, the corresponding abundance map highlights the areas that surround the dark features, particularly on the top of the dune.

3) Weak Bright Source: Endmembers 2, 4, 5, and 6 are identified as belonging to the weak bright source due to a high $R_{1.1}$ and a medium $B_{2.3}$.

Again, the splitting phenomenon affecting this physical source comes from atmospheric and photometric residues. For example, the abundance maps of the endmembers 4 and 5 present the vertical dichotomy detailed in Section IV-B1.

The abundance map obtained by combining the original ones is in agreement with the spatial distribution of the weak bright source extracted by the other methods.

E. Spatial-VCA

The scrutiny of the endmembers extracted by the spatial-VCA algorithm is based on the examination of the corresponding extracted spectra and abundance maps shown in Figs. 6(d) and 10, respectively. Likewise, the spectral parameters are detailed in Table IV and the combined abundance maps are shown in Fig. 11(d).

1) Dark Source: Endmembers 4 and 5 are identified to be related to the dark source due to the lowest $R_{1.1}$ and $B_{2.3}$ among the six endmembers.

Similarly to VCA, the fusion of the two endmembers is justified by spectral and spatial reasons, respectively, the vertical dichotomy and the complementary spectral slopes caused by the atmospheric residue.

Although the combined abundance map is broadly in agreement with the dark sources extracted by the other methods, a slight overestimation of abundance is detected for the upper rows probably due to a persistent residual contribution from the atmosphere.

2) Strong Bright Source: Endmember 3 is recognized as being the strong bright source because of the highest $B_{2.3}$ among all the extracted endmembers and a higher $R_{1.1}$ than for the dark source.

Contrarily to other methods, the associated abundance map shows some differences as the green areas mask the red pixels on some places of the top of the dune. This may come from the penalization of spatially confined sources—such as the dark source—coming from the spatial preprocessing.

3) Weak Bright Source: Endmembers 1, 2, and 6 are associated to the weak bright source due to the highest $R_{1.1}$ and a medium $B_{2.3}$.

This source splitting may come from both atmospheric and photometric residues. The recombination of these three endmembers is justified by the coherence of the resulting abundance map in comparison to other methods.

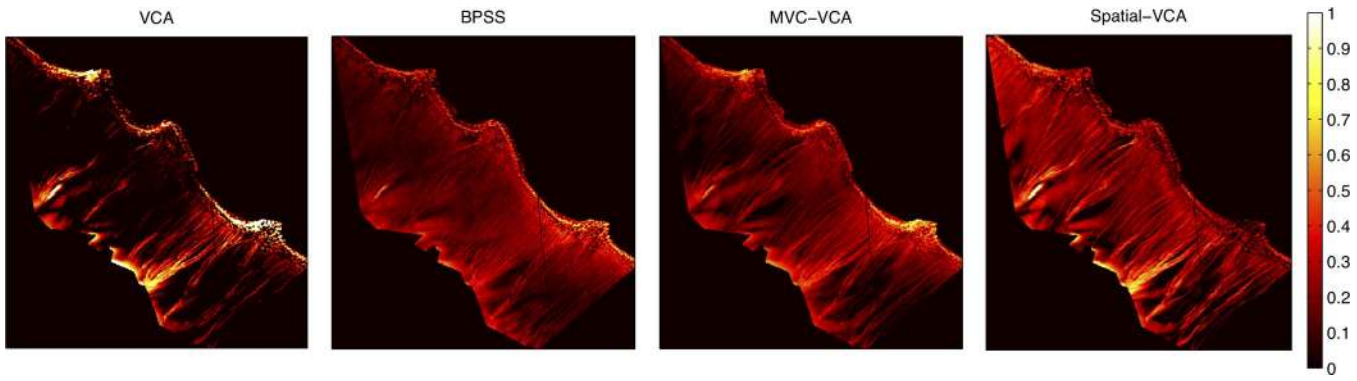

Fig. 12. From left to right, abundance maps corresponding to the dark source extracted by the algorithms VCA, BPSS, MVC-NMF, and spatial-VCA.

V. Validation

In this section, we aim at validating the results obtained by the proposed methodology based on spectral unmixing followed by recombination of the extracted endmembers into meaningful sources. First, Fig. 11 underlines the validity of both processes in a qualitative way as a quite similar relevant planetary scenario is unveiled after interpretation of the color composite images. The notable spatial similarities among the four composite abundance maps represent a cross-validation of the different endmember extraction techniques as well as it validates the corresponding recombination effort. A more in-depth validation is carried out by using the ground truth for the dark source that was introduced in Section II-C. In this matter, abundance maps are validated using the ground truth assuming that the dark features resolved by the HiRISE instrument correspond to the extracted dark source. Unfortunately, reference abundance maps cannot be built for the bright sources from the HiRISE image as they are not distinct by neither markedly different level of apparent reflectance nor structural specificities. Prior to the comparison, the registration procedure (see Section II-C3) is repeated using the same parameter values for the abundance maps provided by the VCA, BPSS, MVC-NMF, and spatial-VCA algorithms. Fig. 12 displays the four maps related to the dark source after cropping them to fit the intersection between the CRISM ROI and the HiRISE image. These products must be compared with the reference map in Fig. 3(b).

Several indicators are used to assess the similarity between the ground truth and the unmixing abundance maps. First, the Pearson correlation coefficient r is computed between both types of abundance maps to measure the similarity as regards to relative spatial distribution. Second, the average value of the absolute error ϵ is computed to complete the quantitative validation. Since misregistration is expected to be one of the main sources of error, several experiments are carried out by calculating r and ϵ according to registration accuracy [see Fig. 4(c)]. In this way, r and ϵ are summarized in Table V by (1) considering all pixels ($mean(r_{reg}) = 0.7$), (2) taking into account only those areas whose associated registration correlation meets $r_{reg} > 0.7$ ($\sim$50% of the pixels with $mean(r_{reg}) = 0.83$), and (3) by selecting the best registered area ($\sim$1% of the pixels with $mean(r_{reg}) = 0.96$). The region corresponding to the third experiment is shown in Fig. 5. A last experiment is performed for the whole population of pixels by computing the distribution of abundance values for the ground truth and the unmixing results (see Fig. 13).

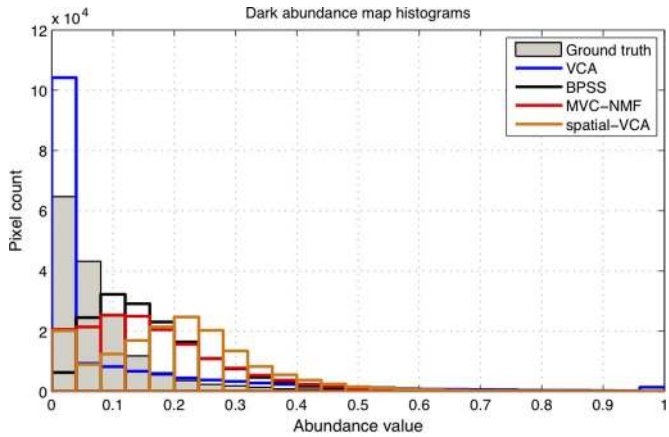

Fig. 13. Distribution of the dark abundances corresponding to the ground truth and the unmixing abundance maps.

In the first experiment, results show a quite good agreement between the unmixing results and the ground truth with r and ϵ values up to 0.69 and down to 0.08, respectively. As regards to correlation, all methods provide notable r values—close to 0.7—except for BPSS, which attains $r = 0.57$. This slight underperformance may be explained by the noisy background of the BPSS dark abundance map displayed in Fig. 12 and may point to a higher sensitivity of this method to the presence of dust. On the other hand, the examination of ϵ reveals that the abundances provided by the spatial-VCA approach are slightly worse with $\epsilon = 0.14$. This bias is mostly originated in the atmospheric residue affecting the upper rows in the form of a small overestimation that is conjugated with a poorer registration accuracy [see Figs. 4(c) and 12]. Contrarily, the average error for other methods is always $\epsilon \leq 0.10$. As for the second experiment, misregistration issues are proved to be an important source of error since the corresponding results outperform those of the first experiment, particularly in terms of r. As a matter of fact, all methods undergo a significant correlation improvement up to 0.06. The improvement of ϵ is less important as this indicator is less sensible to the spatial distribution of the abundance values. In this matter, the best value $\epsilon = 0.08$ seems to represent the intrinsic accuracy of the proposed methodology.

TABLE V
VALIDATION RESULTS REGARDING (1) ALL PIXELS($mean(r_{reg}) = 0.7$), (2) THE MODERATELY WELL-REGISTERED AREAS ($r_{reg} > 0.7$, $mean(r_{reg}) = 0.83$), AND (3) AN IMPROVED REGISTRATION ($mean(r_{reg}) = 0.96$). r IS THE PEARSON CORRELATION COEFFICIENT AND ϵ IS THE AVERAGE VALUE OF THE ABSOLUTE ERROR

Method	VCA		BPSS		MVC-NMF		*spatial*-VCA	
Indicator	r	ϵ	r	ϵ	r	ϵ	r	ϵ
(1) All pixels	0.68	0.08	0.57	0.10	0.69	0.09	0.50	0.14
(2) Accurate registration	0.73	0.08	0.59	0.09	0.72	0.08	0.56	0.13
(3) Best registration	0.81	0.19	0.80	0.13	0.83	0.14	0.77	0.33

Likewise, the third experiment corroborates the improvement tendency according to registration accuracy as r increases up to 0.83 for the MVC-NMF algorithm. Contrarily, the average error is slightly higher in this particular case probably because of the high heterogeneity of the selected area in terms of dark abundance [see Fig. 5(a)] or the presence of nonlinearities coming from the surface. As for the spatial-VCA algorithm, parameter ϵ reveals a notable disagreement with the ground truth that may underline a somewhat faulty extraction of the dark source by this approach.

Several conclusions can be drawn regarding the experiment expressed by Fig. 13. First, the VCA approach underestimates dark abundances in comparison with the ground truth as many pixels correspond to null abundances. This fact may come from the non-positivity and the sum-to-one constraints that result in more restrictive abundance maps. Second, BPSS shows a rather good agreement with the reference abundance map as the abundance distribution only suffers from a small overestimation (average abundance of 0.17 for BPSS and 0.08 for the ground truth). This point underlines the relevance of Fig. 13 since conclusions drawn based on Table V might have indicated an inferior accuracy of BPSS as regardss the other techniques. Third, MVC-NMF presents the best histogram in comparison to the ground truth (average abundance of 0.16) even though a little overestimation is still observed. Eventually, the results of the spatial-VCA approach confirm the initial conclusions drawn according to Table V. As a matter of fact, the dark abundances are generally overestimated with an average abundance of 0.21.

In relation to the small overestimation affecting the majority of the methods, it should be noted that the ground truth may contain slightly underestimated abundances. The reference abundance map generated from the HiRISE image is built by selecting those pixels whose radiance value is much lower than the neighboring pixels. Nonetheless, the dark source may exist in areas classified as brighter ice in the form of a minor dust contamination. The corresponding dust particles may be too small to be resolved spatially by the HiRISE instrument while the corresponding spectral contribution may be strong enough to be detected by the CRISM instrument. As a consequence, the corresponding abundances in the unmixing outcomes would be wrongly considered as being overestimated in comparison to the ground truth. In that case, the average abundance of the ground truth would increase and so would the accuracy of the methods BPSS, MVC-NMF, and spatial-VCA. Another reason to explain the differences between the results coming from the unmixing and the reference may be related to nonlinear contributions and limitations of the endmember extraction methods.

Eventually, an indication of the accuracy of the conducted unmixing is provided by the reconstruction of the original image with the estimated endmembers and their associated abundances. This is done by using the linear mixture model to approximate each pixel by the corresponding linear combination of endmembers weighted by the estimated abundances. By doing this, the average reconstruction error of the image [i.e., the term $\mathbf{e}$ in (1)] is calculated by means of the signal-to-noise ratio as 36 dB for VCA, 41 dB for BPSS, 43 dB for MVC-NMF, and 35 dB for spatial-VCA. These results show a very satisfactory reconstruction by all methods, BPSS and MVC-NMF particularly. After inspection of the signal-to-noise ratio maps, the reconstruction error was found to be very homogeneous with no pixels under 30 dB. These results are an additional proof that the linear model is indeed relevant and may be valuable in future research to locate those confined areas with slightly higher reconstruction errors that may point to nonlinear effects.

VI. CONCLUSIONS

In this paper, we have carried out validation and intercomparison of a comprehensive selection of state-of-the-art spectral unmixing techniques applied on planetary hyperspectral data. An appropriate case study has been defined by choosing a hyperspectral image acquired by the CRISM instrument displaying the Russell dune. This particular area of Mars is suitable for testing the benefits of spectral unmixing under a linear model because of the coexistence of two distinct materials—dark features and brighter ice—resulting in geographic subpixel mixtures at the CRISM resolution.

First, while two methods were considered for evaluating the number of endmembers in the test image only the ELM technique provided a realistic input for the subsequent endmember extraction. Then, spectral signatures extracted by the selected unmixing techniques were characterized and examined by spectral indicators to ensure their physical correctness. As a result, the initially selected methods N-FINDR, MVES, and SISAL were discarded due to unsatisfactory results. By contrast, the techniques VCA, BPSS, MVC-NMF, and spatial-VCA revealed the same three physically meaningful sources. An effort of recombination was however required due to repeated splitting of physical sources into a few endmembers caused by residual nonlinearities. For that purpose, the spectral indicators were considered together with spatial correlations among the endmember abundance maps. In that matter, we noted that spectra belonging to the physical sources are better reconstructed from endmembers extracted by the VCA and spatial-VCA methods

due to the pure pixel assumption. Exhaustive evaluation of the unmixing outcomes was also conducted by comparison of derived abundance maps with a reference. In that matter, very high-resolution HiRISE imagery and geomorphological techniques were used to generate a reference abundance map for the physical source related to the dark features happening in the Russell dune.

The quality of the results is estimated through several indicators— the correlation coefficient and average error between the reconstructed abundance maps and the groud truth and the superposition of the abundance distributions by means of the corresponding histograms. To our knowledge, this quantitative assessment represents the very first attempt to validate abundance maps produced by spectral unmixing of real data in an independent and quantitative manner. In that matter, global and local comparisons show that misregistration inaccuracies between the HiRISE and CRISM images represent the major source of error. For the best registered areas, the MVC-NMF and VCA methods outperform the BPSS and spatial-VCA techniques in terms of correlation coefficient. This ranking is however put into perspective after considering the average error and, particularly, the distribution of abundance values and average reconstruction error. As a matter of fact, BPSS shows significantly better performances than stated by the correlation indicator, agreeing quite satisfactorily with the reference histogram and showing the second lowest reconstruction error in terms of signal-to-noise ratio. On the other hand, the first position of the MVC-NMF method is never questioned since it generally provides the best results. As for the spatial-VCA, experimental results point to slightly lower performances which are probably due to the inherent penalization of the spatial preprocessing as for spatially confined sources such as the dark features on the Russell dune [21]. Eventually, the side effect of imposing the positivity and sum-to-one constrains turns into a lack of sensitivity, particularly in the VCA case, in the form of extremely low dark abundances frequently set to zero. As matter of fact, the abundance constraints might be less relevant in our case since physical sources—related to positive abundance values—are obtained after recombination of initial endmembers.

We conclude that abundance maps provided by VCA, BPSS, and MVC-NMF are generally accurate, i.e., sufficient for an initial planetary interpretation. In this matter, the results given by VCA and MVC-NMF—rather than BPSS which is much more computer intensive—can be considered as a primary quick look that helps revealing physical sources in the scene of study together with subtle residues of instrumental or atmospheric corrections. As a matter of fact, unmixing results may be used to iteratively drive the improvement of the image preprocessing, which has proved to be critical as for the existence of nonlinearities in this paper. As regards to the pure pixel assumption, the algorithms BPSS and MVC-NMF seem to outperform the VCA-based approaches in terms of estimated abundances while the latter extract more physically coherent spectra. An issue deserving further research would be to evaluate the risks of extracting unphysical endmembers when performing unmixing with BPSS and MVC-NMF as it happens for the MVES and SISAL algorithms.

Although examination of the HiRISE image and experimental results regarding reconstruction error confirm the linear mixing hypothesis in our case, some residual nonlinearities may prevail. Major causes are (i) intrinsic variability of the physical sources, (ii) nonlinear mixing at the grain size scale, and (iii) adjacency effects due to multiple scattering between the atmosphere and the surface. All these factors may be related to uncertainties affecting the abundance maps provided by spectral unmixing. In order to take into account existent nonlinearities and improve the accuracy of the results, linear unmixing must be followed by a complete physical analysis of the image through the inversion of a physical model. First, simulating the spectra of the physical sources with radiative transfer algorithms will allow building a comprehensive physical model of the scene with some free parameters including the source abundances. Second, model inversion will be performed for all CRISM spectra using the estimated abundance maps as the most probable solution. By doing this, the risk of multiple solutions will be diminished as regards to the improved abundance maps.

ACKNOWLEDGMENT

The authors would like to thank the anonymous reviewers for their constructive comments that helped improving this paper.

REFERENCES

[1] S. Murchie, R. Arvidson, P. Bedini, K. Beisser, J.-P. Bibring, J. Bishop, J. Boldt, P. Cavender, T. Choo, R. T. Clancy, E. H. Darlington, D. Des Marais, R. Espiritu, D. Fort, R. Green, E. Guinness, J. Hayes, C. Hash, K. Heffernan, J. Hemmler, G. Heyler, D. Humm, J. Hutcheson, N. Izenberg, R. Lee, J. Lees, D. Lohr, E. Malaret, T. Martin, J. A. McGovern, P. McGuire, R. Morris, J. Mustard, S. Pelkey, E. Rhodes, M. Robinson, T. Roush, E. Schaefer, G. Seagrave, F. Seelos, P. Silverglate, S. Slavney, M. Smith, W.-J. Shyong, K. Strohbehn, H. Taylor, P. Thompson, B. Tossman, M. Wirzburger, and M. Wolff, "Compact Reconnaissance Imaging Spectrometer for Mars (CRISM) on Mars Reconnaissance Orbiter (MRO)," *J. Geophys. Res. (Planets)*, vol. 112, no. E05, p. E05 S03, 2007.

[2] Eur. Space Agency, ESA SP-1240 J.-P. Bibring, A. Soufflot, M. Berthé, Y. Langevin, B. Gondet, P. Drossart, M. Bouyé, M. Combes, P. Puget, A. Semery, G. Bellucci, V. Formisano, V. Moroz, and V. Kottsov, "OMEGA: Observatoire pour la Minéralogie, l'Eau, les Glaces et l'Activité," Mars Express: The Scientific Payload, Noordwijk, The Netherlands, Aug. 2004, ESA SP-1240.

[3] P. Drossart, G. Piccioni, A. Adriani, F. Angrilli, G. Arnold, K. H. Baines, G. Bellucci, J. Benkhoff, B. Bézard, J.-P. Bibring, A. Blanco, M. I. Blecka, R. W. Carlson, A. Coradini, A. di Lellis, T. Encrenaz, S. Erard, S. Fonti, V. Formisano, T. Fouchet, R. Garcia, R. Haus, J. Helbert, N. I. Ignatiev, P. G. J. Irwin, Y. Langevin, S. Lebonnois, M. A. Lopez-Valverde, D. Luz, L. Marinangeli, V. Orofino, A. V. Rodin, M. C. Roos-Serote, B. Saggin, A. Sanchez-Lavega, D. M. Stam, F. W. Taylor, D. Titov, G. Visconti, M. Zambelli, R. Hueso, C. C. C. Tsang, C. F. Wilson, and T. Z. Afanasenko, "Scientific goals for the observation of Venus by VIRTIS on ESA/Venus express mission," *Planet. Space Sci.*, vol. 55, no. 12, pp. 1653–1672, Oct. 2007.

[4] R. W. Carlson, P. R. Weissman, W. D. Smythe, and J. C. Mahoney, "Near-infrared mapping spectrometer experiment on Galileo," *Space Sci. Rev.*, vol. 60, no. 1–4, pp. 457–502, May 1992.

[5] R. H. Brown, K. H. Baines, G. Bellucci, J.-P. Bibring, B. J. Buratti, F. Capaccioni, P. Cerroni, R. N. Clark, A. Coradini, D. P. Cruikshank, P. Drossart, V. Formisano, R. Jaumann, Y. Langevin, D. L. Matson, T. B. McCord, V. Mennella, E. Miller, R. M. Nelson, P. D. Nicholson, B. Sicardy, and C. Sotin, "The Cassini Visual and Infrared Mapping Spectrometer (VIMS) investigation," *Space Sci. Rev.*, vol. 115, no. 1–4, pp. 111–168, Dec. 2004.

[6] O. Forni, F. Poulet, J.-P. Bibring, S. Erard, C. Gomez, Y. Langevin, and B. Gondet, "Component separation of OMEGA spectra with ICA," in *Proc. 36th Lunar Planet. Sci. Conf.*, 2005, p. 1623.
[7] S. Erard, P. Drossart, and G. Piccioni, "Multivariate analysis of Visible and Infrared Thermal Imaging Spectrometer (VIRTIS) Venus Express nightside and limb observations," *J. Geophys. Res. (Planets)*, vol. 114, no. E00, p. E00 B27, 2009.
[8] J. M. P. Nascimento, "Does independent component analysis play a role in unmixing hyperspectral data?" *IEEE Trans. Geosci. Remote Sens.*, vol. 43, no. 1, pp. 175–187, Jan. 2005.
[9] D. D. Lee and H. S. Seung, "Learning the parts of objects by non-negative matrix factorization," *Nature*, vol. 401, no. 6755, pp. 788–791, Oct. 1999.
[10] M. Parente, J. L. Bishop, and J. F. Bell, III, "Spectral unmixing for mineral identification in pancam images of soils in Gusev crater, Mars," *Icarus*, vol. 203, no. 2, pp. 421–436, Oct. 2009.
[11] S. Moussaoui, D. Brie, A. Mohammad-Djafari, and C. Carteret, "Separation of non-negative mixture of non-negative sources using a Bayesian approach and MCMC sampling," *IEEE Trans. Signal Process.*, vol. 54, no. 11, pp. 4133–4145, Nov. 2006.
[12] S. Moussaoui, H. Hauksdóttir, F. Schmidt, C. Jutten, J. Chanussot, D. Brie, S. Douté, and J. A. Benediktsson, "On the decomposition of Mars hyperspectral data by ICA and Bayesian positive source separation," *Neurocomputing*, vol. 71, no. 10–12, pp. 2194–2208, Jun. 2008.
[13] J. M. P. Nascimento and J. M. B. Dias, "Vertex component analysis: A fast algorithm to unmix hyperspectral data," *IEEE Trans. Geosci. Remote Sens.*, vol. 43, no. 4, pp. 898–910, Apr. 2005.
[14] B. Luo and J. Chanussot, "Unsupervised hyperspectral image classification by using linear unmixing," in *Proc. 16th IEEE Int. Conf. Image Process.*, Cairo, Egypt, 2009, pp. 2877–2880.
[15] M. E. Winter, "Fast autonomous spectral end-member determination in hyperspectral data," in *Proc. 13th Int. Conf. Appl. Geologic Remote Sens.*, Vancouver, BC, Canada, 1999, vol. II, pp. 337–344.
[16] D. R. Thompson, L. Mandrake, M. S. Gilmore, and R. Castano, "Superpixel endmember detection," *IEEE Trans. Geosci. Remote Sens.*, vol. 48, no. 11, pp. 4023–4032, Nov. 2010.
[17] L. Miao and H. Qi, "Endmember extraction from highly mixed data using minimum volume constrained non-negative matrix factorization," *IEEE Trans. Geosci. Remote Sens.*, vol. 45, no. 3, pp. 765–777, Mar. 2007.
[18] T.-H. Chan, C.-Y. Chi, Y.-M. Huang, and W.-K. Ma, "A convex analysisbased minimum-volume enclosing simplex algorithm for hyperspectral unmixing," *IEEE Trans. Signal Process.*, vol. 57, no. 11, pp. 4418–4432, Nov. 2009.
[19] J. Bioucas-Dias, "A variable splitting augmented Lagrangian approach to linear spectral unmixing," in *Proc. 1st IEEE Workshop Hyperspectral Image Signal Process.: Evolution Remote Sens.*, Grenoble, France, Aug. 2009, pp. 1–4.
[20] S. Jia and Y. Qian, "Spectral and spatial complexity-based hyperspectral unmixing," *IEEE Trans. Geosci. Remote Sens.*, vol. 45, no. 12, pp. 3867–3879, Dec. 2007.
[21] M. Zortea and A. Plaza, "Spatial preprocessing for endmember extraction," *IEEE Trans. Geosci. Remote Sens.*, vol. 47, no. 8, pp. 2679–2693, Aug. 2009.
[22] P. Debba, E. J. M. Carranza, F. D. van der Meer, and A. Stein, "Abundance estimation of spectrally similar minerals by using derivative spectra in simulated annealing," *IEEE Trans. Geosci. Remote Sens.*, vol. 44, no. 12, pp. 3649–3658, Dec. 2006.
[23] A. Zare and P. Gader, "PCE: Piecewise convex endmember detection," *IEEE Trans. Geosci. Remote Sens.*, vol. 48, no. 6, pp. 2620–2632, Jun. 2010.
[24] S. Jia and Y. Qian, "Constrained non-negative matrix factorization for hyperspectral unmixing," *IEEE Trans. Geosci. Remote Sens.*, vol. 47, no. 1, pp. 161–173, Jan. 2009.
[25] E. Gardin, P. Allemand, C. Quantin, and P. Thollot, "Defrosting, dark flow features, and dune activity on Mars: Example in Russell crater," *J. Geophys. Res.*, vol. 115, no. E06, p. E06 016, 2010.
[26] M. Parente, "A new approach to denoising CRISM images," in *Proc. 39th Lunar Planet. Sci. Conf.*, 2008, p. 2528.
[27] X. Ceamanos and S. Douté, "Spectral smile correction of CRISM/MRO hyperspectral images," *IEEE Trans. Geosci. Remote Sens.*, vol. 48, no. 11, pp. 3951–3959, Nov. 2010.
[28] S. Douté, "Retrieving Mars surface reflectance from OMEGA/MEX imagery," in *Proc. 1st IEEE Workshop Hyperspectral Image Signal Process.: Evolution Remote Sens.*, Grenoble, France, Aug. 2009, pp. 1–4.
[29] S. Douté and X. Ceamanos, "Retrieving Mars aerosol optical depth from CRISM/MRO imagery," in *Proc. 2nd IEEE Workshop Hyperspectral Image Signal Process.: Evolution Remote Sens.*, Reykjavik, Iceland, Jun. 2010, pp. 1–4.
[30] P. C. McGuire, J. L. Bishop, A. J. Brown, A. A. Fraeman, G. A. Marzo, M. F. Morgan, S. L. Murchie, J. F. Mustard, M. Parente, S. M. Pelkey, T. L. Roush, F. P. Seelos, M. D. Smith, L. Wendt, and M. J. Wolff, "An improvement to the volcano-scan algorithm for atmospheric correction of CRISM and OMEGA spectral data," *Planet. Space Sci.*, vol. 57, no. 7, pp. 809–815, Jun. 2009.
[31] A. S. McEwen, E. M. Eliason, J. W. Bergstrom, N. T. Bridges, C. J. Hansen, W. A. Delamere, J. A. Grant, V. C. Gulick, K. E. Herkenhoff, L. Keszthelyi, R. L. Kirk, M. T. Mellon, S. W. Squyres, N. Thomas, and C. M. Weitz, "Mars Reconnaissance Orbiter's High Resolution Imaging Science Experiment (HiRISE)," *J. Geophys. Res. (Planets)*, vol. 112, no. E5, p. E05 S02, 2007.
[32] J. A. Richards and X. Jia, *Remote Sensing Digital Image Analysis*. Berlin, Germany: Springer-Verlag, 1999.
[33] E. F. Vermote, N. El Saleous, C. O. Justice, Y. J. Kaufman, J. L. Privette, L. Remer, J. C. Roger, and D. Tanré, "Atmospheric correction of visible to middle-infrared EOS-MODIS data over land surfaces: Background, operational algorithm and validation," *J. Geophys. Res.*, vol. 102, no. D14, pp. 17 131–17 141, 1997.
[34] J. M. Bioucas-Dias and J. M. Nascimento, "Hyperspectral subspace identification," *IEEE Trans. Geosci. Remote Sens.*, vol. 46, no. 8, pp. 2435–2445, Aug. 2008.
[35] N. Dobigeon, S. Moussaoui, J.-Y. Tourneret, and C. Carteret, "Bayesian separation of spectral sources under non-negativity and full additivity constraints," *Signal Process.*, vol. 89, no. 12, pp. 2657–2669, Dec. 2009.
[36] F. Schmidt, A. Schmidt, E. Tréguier, and M. Guiheneuf, "Implementation strategies for hyperspectral unmixing using Bayesian source separation," *IEEE Trans. Geosci. Remote Sens.*, vol. 48, no. 11, pp. 4003–4013, Nov. 2010.

Xavier Ceamanos (S'09) received the M.Sc. degree in electrical engineering from the Universitat Politècnica de Catalunya (UPC), Barcelona, Spain, in 2007, and from the Grenoble Institute of Technology (Grenoble INP), Grenoble, France, in 2008. He is currently working toward the Ph.D. degree at the Institut de Planétologie et d'Astrophysique de Grenoble (Centre National de la Recherche Scientifique-Université Joseph Fourier), Grenoble, France. His Ph.D. work is devoted to developing statistical and physical methods for analyzing remotely sensed hyperspectral images. In particular, he is working with multi-angular hyperspectral data acquired by the CRISM/MRO spectrometer (NASA).

His research interests include calibration and processing of data acquired by imaging spectrometers, spectral unmixing techniques, and atmospheric correction and inversion algorithms to retrieve surface reflectance from top-of-atmosphere radiances.

Sylvain Douté received the M.Sc. degree in physics from the Université Joseph Fourier (UJF), Grenoble, France, in 1994, and the Ph.D. degree in remote sensing from the Université Denis Diderot, Paris, France. His Ph.D. work was devoted to modeling light scattering properties of planetary icy surfaces with application to the study of Io and Pluto.

He held a postdoctoral position for two years at the Institute of Geophysics and Planetary Physics (University of California, Los Angeles) to analyze images of the Galilean satellites acquired by the near-infrared mapping spectrometer Galileo (NASA). He is currently a Researcher in planetary physics at the Institut de Planétologie et d'Astrophysique de Grenoble (Centre National de la Recherche Scientifique-UJF), Grenoble. His research interests are directed toward the study of Mars cryosphere and polar atmosphere by imaging spectroscopy thanks to his status of co-investigator regarded the spatial OMEGA/MEX and CRISM/MRO experiments. This research is supported by R&T activities in hyperspectral image post-processing and analysis carried out in the framework of the Vahiné project led by Dr. Douté. Physical models, statistical inversion technics, as well as signal processing methods are developed in this framework.

Dr. Douté is a member of the "Programme National de Planétologie" science committee and of the American Geophysical Union.

Bin Luo received the M.Sc. degree from École Normale Supérieure (ENS) Cachan, France, and the Ph.D. degree from École Nationale Supérieure de Telecommunication (ENST) Paris, France, in 2007.

He worked as Postdoctoral Researcher at Gipsa-lab, Grenoble Institute of Technology (Grenoble INP), Grenoble, France, from 2008 to 2010. He is currently an Associate Professor at the Laboratory of Information Engineering in Surveying, Mapping and Remote Sensing (LIESMARS), Wuhan University, Wuhan, China. His research interests include hyperspectral data analysis, high-resolution image processing, and indexation of images at different resolutions.

Frédéric Schmidt received the Ph.D. degree from the Laboratoire de Planétologie de Grenoble (Centre National de la Recherche Scientifique-Université Joseph Fourier), Grenoble, France, in 2007.

He spent two years at the European Space Astronomy Centre, European Space Agency (ESA), Madrid, Spain, as a Postdoctoral Fellow. Since 2009, he has been an Assistant Professor with the Laboratoire Intéractions et Dynamique des Environnements de Surface, University Paris-Sud, Orsay, France, and is also with the Centre National de la Recherche Scientifique. He is a Co-investigator of the OMEGA imaging spectrometer onboard Mars Express (ESA). His research interests are in analysis of hyperspectral data, ices, and polar processes on planet Mars.

Gwenaël Jouannic received the M.Sc. degree in earth sciences from the Université Pierre et Marie Curie, Paris, France, in 2009. He is currently working toward the Ph.D. degree in the team "Géomorphologie planétaire" in the Laboratoire Intéractions et Dynamiques des Environnements de Surface, Université Paris-Sud, Orsay, France. His Ph.D. work is devoted to the geomorphological study of Martian debris flows on dunes. In particular, he is working with High-Resolution Imaging Science Experiment (HiRISE) images and high-resolution Digital Topographic Models in order to better characterize 3-D geometry of Martian debris flows.

His research interests include the seasonal processes on Mars as present flow activities currently observed on Martian dunes slopes.

Jocelyn Chanussot (SM'04) received the M.Sc. degree in electrical engineering from the Grenoble Institute of Technology (Grenoble INP), Grenoble, France, in 1995, and the Ph.D. degree from Savoie University, Annecy, France, in 1998.

In 1999, he was with the Geography Imagery Perception Laboratory for the Délégation Générale de l'Armement (DGA—French National Defense Department). Since 1999, he has been with Grenoble INP, where he was an Assistant Professor from 1999 to 2005, an Associate Professor from 2005 to 2007, and is currently a Professor of signal and image processing. He is currently conducting his research at the Grenoble Images Speech Signals and Automatics Laboratory (GIPSA-Lab). His research interests include image analysis, multicomponent image processing, nonlinear filtering, and data fusion in remote sensing.

Dr. Chanussot is the founding President of IEEE Geoscience and Remote Sensing French chapter (2007–2010) which received the 2010 IEEE GRS-S Chapter Excellence Award "for excellence as a Geoscience and Remote Sensing Society chapter demonstrated by exemplary activities during 2009". He was a member of the IEEE Geoscience and Remote Sensing AdCom (2009–2010), in charge of membership development. He was the General Chair of the first IEEE GRSS Workshop on Hyperspectral Image and Signal Processing, Evolution in Remote sensing (WHISPERS). He is the Chair (2009–2011) and was the Cochair of the GRS Data Fusion Technical Committee (2005–2008). He was a member of the Machine Learning for Signal Processing Technical Committee of the IEEE Signal Processing Society (2006–2008) and the Program Chair of the IEEE International Workshop on Machine Learning for Signal Processing, (2009). He was an Associate Editor for the IEEE GEOSCIENCE AND REMOTE SENSING LETTERS (2005–2007) and for *Pattern Recognition* (2006–2008). Since 2007, he is an Associate Editor for the IEEE TRANSACTIONS ON GEOSCIENCE AND REMOTE SENSING. Since 2011, he has been the Editor-in-Chief of the IEEE JOURNAL OF SELECTED TOPICS IN APPLIED EARTH OBSERVATIONS AND REMOTE SENSING.